

A neural network machine-learning approach for characterising hydrogen trapping parameters from TDS experiments

Nicoletta Marrani^{ID}, Tim Hageman^{ID}*, Emilio Martínez-Pañeda^{ID}*

Department of Engineering Science, University of Oxford, Oxford OX1 3PJ, UK

ARTICLE INFO

Dataset link: https://github.com/nicolettamarrani/TDS_ML_Approach.git, <https://mechmat.ox.ac.uk/codes>

Keywords:

Hydrogen
Thermal desorption spectroscopy
Trapping
Parameter identification
Machine learning
Neural network

ABSTRACT

The hydrogen trapping behaviour of metallic alloys is generally characterised using Thermal Desorption Spectroscopy (TDS). However, as an indirect method, extracting key parameters (trap binding energies and densities) remains a significant challenge. To address these limitations, this work introduces a machine learning-based scheme for parameter identification from TDS spectra. A multi-Neural Network (NN) model is developed and trained exclusively on synthetic data to predict trapping parameters directly from experimental data. The model comprises two multi-layer, fully connected, feed-forward NNs trained with backpropagation. The first network (classification model) predicts the number of distinct trap types. The second network (regression model) then predicts the corresponding trap densities and binding energies. The NN architectures, hyperparameters, and data pre-processing were optimised to minimise the amount of training data. The proposed model demonstrated strong predictive capabilities when applied to three tempered martensitic steels of different compositions. The code developed is freely provided.

1. Introduction

To transition away from fossil fuels as the primary energy source, the global energy industry has increasingly focused on developing low-carbon technologies. Alongside the widespread adoption of renewable energy, hydrogen is gaining prominence as both a fuel and an energy carrier [1–3]. Its natural abundance and low projected environmental impact position hydrogen as a promising solution for decarbonising traditionally hard-to-abate industries [4,5]. However, the development of a hydrogen-based economy is hindered by hydrogen's tendency to degrade the mechanical properties of structural materials—a phenomenon known as hydrogen embrittlement [6]. A detailed understanding of hydrogen embrittlement is necessary before existing energy infrastructure, such as gas pipelines, is adapted to transport hydrogen [7,8], with one of the main limitations being the characterisation of metal properties.

Despite extensive experimental and computational efforts to understand the mechanisms of hydrogen embrittlement, characterising the properties of metals and predicting their degradation due to hydrogen remains a challenge [9]. These predictions require a thorough examination of hydrogen–metal interactions, including ingress [10–13], diffusion through the lattice [14,15], and trapping at microstructural imperfections [16–18]. In particular, the rapid diffusion of hydrogen

through the metal lattice and its subsequent trapping at crystal defects have been identified as key factors influencing susceptibility to hydrogen embrittlement [6,19].

One well-established technique for characterising hydrogen trapping behaviour in metallic alloys is Thermal Desorption Spectroscopy (TDS) [20], also referred to as Thermal Desorption Analysis (TDA). TDS analysis has been used extensively to understand how microstructural features—such as vacancies [21], dislocations [22–24], grain boundaries [25], voids [26–28], and precipitates [29–31]—interact with and retain hydrogen. Each of these features, commonly referred to as traps, is characterised by a unique binding energy and trap density, which TDS can quantify. The technique is valuable for comparing hydrogen trapping across materials and examining the influence of environmental and processing factors, such as variations in hydrogen charging conditions [32] and tempering temperature [22,33]. Additionally, TDS can be combined with other techniques, such as X-ray diffraction and microstructural analysis, to investigate hydrogen trapping mechanisms in different crystal structures [34].

Although TDS is a powerful tool for probing trapping properties, it is an indirect method, and extracting critical parameters, such as trap binding energies and densities, requires careful post-processing and interpretation of the desorption spectrum [35]. As TDS obtains the desorption spectrum of all the traps combined, this combined spectrum

* Corresponding authors.

E-mail addresses: tim.hageman@eng.ox.ac.uk (T. Hageman), emilio.martinez-paneda@eng.ox.ac.uk (E. Martínez-Pañeda).

needs to be split into contributions of individual traps [20]. Kissinger's first-order rate theory [36] is the simplest framework for evaluating TDS spectra, commonly applied through the Choo-Lee approach [25]. While Kissinger's method is popular for its simplicity, it has limitations, primarily due to assumptions of infinitely fast hydrogen diffusion and neglecting the role of multiple interacting trapping mechanisms. Consequently, it is only valid for TDS tests on fast diffusion materials (e.g., bcc alloys), using very thin samples, and at very slow heating rates [37].

An alternative framework, proposed by McNabb and Foster [38], accounts for the role of trapping and de-trapping in hydrogen diffusion. It assumes sparsely distributed, isolated traps and requires numerical methods for solving the system of coupled differential equations. This framework can be simplified using Oriani's approach [39], which assumes equilibrium between hydrogen in the lattice and trapping sites, and which generally applies, especially for low trap occupancies [40]. A number of studies have used these hydrogen diffusion-trapping models, using finite difference [41] and finite element methods [37,42] to solve the resulting PDEs, considering both single and multi-trap scenarios [43–46]. Garcia-Macias et al. [43] developed TDS Simulator, a MATLAB App capable of modelling TDS experiments for any material and test parameters, and extracting trapping characteristics (the number of traps, binding energies, and densities) from experimental desorption curves. They implemented the McNabb-Foster and Oriani frameworks for multiple trap sites, using a deterministic parameter inference algorithm based on particle swarm optimisation for data fitting. Delaporte-Mathurin et al. [47] developed a finite element code for hydrogen transport simulations. Using the Nelder–Mead algorithm and parametric optimisation, they determined the trapping characteristics of materials like Aluminium, Tungsten, EURO-FER, and Beryllium. This method successfully extracted trapping parameters from experimental TDS spectra. Drexler et al. [48] used a trap-diffusion finite element model-based evaluation procedure to extract the trapping quantities of interest from the TDS spectra of two Fe-C-Ti alloys. The developed optimisation routine was able to successfully predict both the trapping parameters, i.e. binding energy and density, and the initial hydrogen concentration of the two alloys. However, all these approaches have limitations: they require defining *a priori* the number of traps, which could lead to unsatisfactory fits even if the algorithm converges. Additionally, as these methods rely on conventional optimisation algorithms, they require the initial estimates of the trapping energy and density to be close to the correct values, as otherwise the algorithm can converge to local minima, preventing the correct material parameters from being predicted. Finally, they require large amounts of simulations to be performed every time the parameters are fitted, with this simulation effort not being able to be reused for future predictions. This work aims to overcome these limitations using ML approaches.

Growth in computing power has led to the development of Artificial Intelligence (AI), a powerful tool now used in numerous fields, including natural language processing, image recognition, finance, medicine, and material science [49–52]. Machine learning (ML), a branch of AI, uses methods such as decision trees, linear regression, and artificial neural networks (ANNs) to extract knowledge from data, learn from it, and solve complex problems [50]. Recently, deep learning, a subset of ML, has emerged as a prominent tool, utilising deep ANNs to address highly complex issues. Deep learning models excel in analysing large datasets and are particularly effective when large amounts of data are available [53].

ANNs are increasingly used in material science and engineering [54–56], and their use has recently been extended to the analysis of hydrogen–material interactions [57–60]. However, they are yet to be employed to infer trapping characteristics from TDS output. Due to the vast amount of training data that can easily be generated through numerical simulations, employing deep artificial neural networks is suitable for addressing the complexity of the interpretation of TDS

spectra. The objective of this work is to introduce a machine learning-based scheme for parameter identification from TDS experiments. The aim is to have this ANN trained solely on simulated data, while being accurate in predicting parameters from experimental data. Hence, we present an ML-based framework to predict the number of trap types and the corresponding binding energies and densities from experimental TDS spectra, without needing to provide the number of different trap types and an initial estimate of the binding energies and densities. Furthermore, by using neural networks, training data can be generated *a priori* and reused across experiments to efficiently and quickly identify traps without needing any manual post-processing steps, accelerating the capabilities of TDS to characterise the hydrogen trapping properties of metals.

The remainder of this paper is organised as follows. First, the hydrogen transport model is introduced in Section 2, including the governing equations and its finite element method (FEM) implementation. Next, the machine learning methodology is described in Section 3, outlining the architecture of the multi-NN model, the model optimisation process, and the generation of training data using FEM simulations. Finally, the performance of the proposed multi-NN model approach is demonstrated through three case studies involving tempered martensitic steels of different composition in Section 4. The paper concludes with a discussion of the approach limitations and main advantages.

2. Hydrogen transport model

In order to generate the training data and verify the correctness of the ANN predictions, a numerical model based on the finite element method was developed to simulate TDS spectra for an arbitrary choice of material and test parameters. Upon ingress into the metal, hydrogen diffuses through the crystal lattice by hopping between normal interstitial lattice sites (NILS). As the hydrogen diffuses through the crystal lattice, it can be captured by micro-structural heterogeneities, known as traps. Thus, the total hydrogen concentration C is the sum of the lattice hydrogen concentration C_L and the trapped hydrogen concentration C_T . Within the finite element model, the lattice and trapped concentrations are used as degrees of freedom to be solved for.

In TDS experiments, the hydrogen desorption rate is measured from a plate of thickness L that has been uniformly pre-charged to achieve a homogeneously distributed hydrogen concentration of C_L^0 . After an initial rest period t_{rest} (in which the sample is held at room temperature and transferred from the hydrogen charging device to the TDS setup), heating takes place at a constant heating rate ϕ , causing the temperature of the sample to rise from T_{min} to T_{max} and desorption to occur as the trapped hydrogen is released. The temperature T at any time t during the TDS test is defined as,

$$T = T_{\text{min}} + \phi \langle t - t_{\text{rest}} \rangle, \quad (1)$$

where the Macaulay brackets $\langle \cdot \rangle$ ($\langle x \rangle = x$ if $x \geq 0$, otherwise $\langle x \rangle = 0$) are used to indicate an initial period t_{rest} where the temperature is held constant at T_{min} , the initial temperature (293.15 K, typically). We assume that the heating rate ϕ is sufficiently slow compared to the rate of heat transfer, such that the temperature distribution $T(t)$ is assumed to be spatially uniform throughout the TDS sample. Given that the sample thickness is significantly smaller than all other dimensions, desorption primarily occurs at the surfaces corresponding to $x = \pm L/2$; consequently, the problem is effectively one-dimensional. As the temperature rises, the lattice hydrogen concentration C_L evolves spatially and temporally as shown in Fig. 1(b). A flux profile similar to that in Fig. 1(c) is obtained.

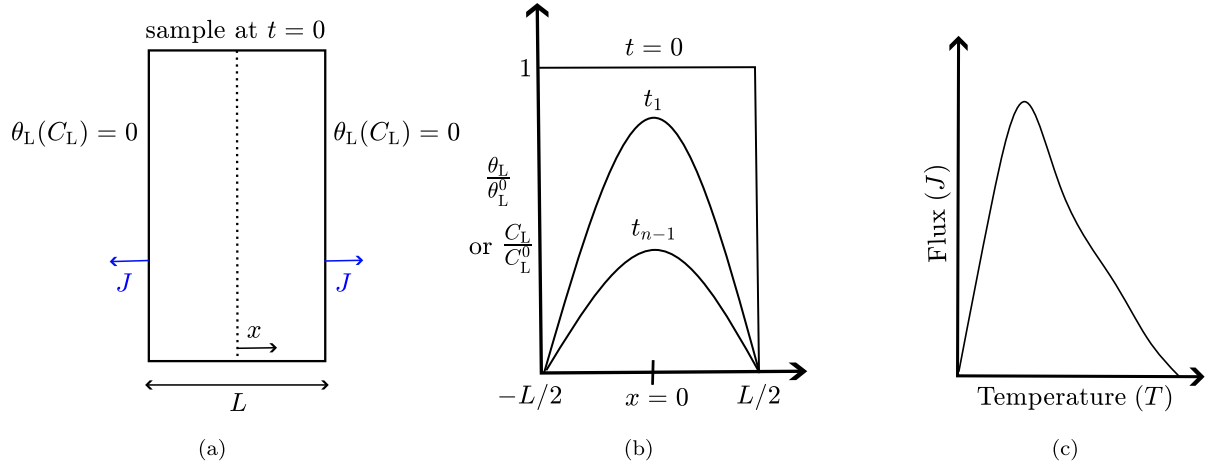


Fig. 1. Thermal Desorption Spectroscopy (TDS) experiments. (a) Schematic illustration of the sample geometry, initial and boundary conditions in a TDS test. (b) Transient solution curves of the normalised lattice occupancy fraction θ_L/θ_L^0 (or C_L/C_L^0) along the sample thickness L at different times t . (c) Schematic of a typical hydrogen desorption flux curve (flux versus temperature) obtained in a TDS test.

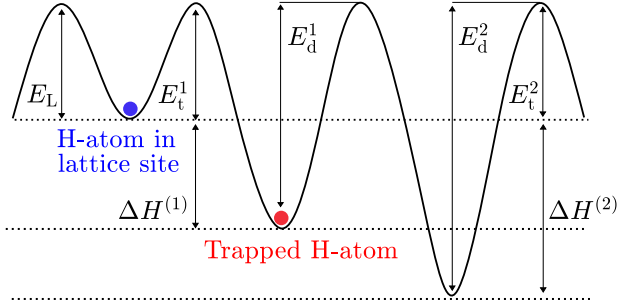


Fig. 2. Overview of different energy levels associated with hydrogen diffusion in metals. E_L is the interstitial lattice activation energy, $E_t (>0)$ is the trapping activation energy and $E_d (>0)$ is the de-trapping activation energy. It is generally assumed that $E_t \approx E_L$, and E_d and E_t define the binding energy $\Delta H (<0)$ via $\Delta H = E_t - E_d$.

2.1. Governing equations

The diffusive transport of the hydrogen lattice concentration $C_L(x, t)$ over the NILS is dictated by Fick's Law, adjusted to account for the possibility of trapping and de-trapping. Assuming there are n_t types of traps, Fick's second law can be written as:

$$\frac{\partial C_L}{\partial t} + \sum_{i=1}^{n_t} \frac{\partial C_T^i}{\partial t} = D_L \frac{\partial^2 C_L}{\partial x^2} \quad (2)$$

where C_L and C_T are the lattice hydrogen concentration and the trapped hydrogen concentration, respectively, and D_L is the lattice diffusion coefficient. This lattice diffusion coefficient depends on the temperature T of the sample via the following Arrhenius law:

$$D_L = D_0 \exp\left(-\frac{E_L}{RT}\right) \quad (3)$$

with D_0 is the pre-exponential factor for lattice diffusion, E_L is the activation energy of the lattice sites (in J/mol), and R the universal gas constant. Eq. (2) can be reformulated considering the standard definitions of density of lattice sites, N_L , density of trapping sites for a trap type, $N_T^{(i)}$, lattice occupancy, $0 \leq \theta_L \leq 1$, and trap occupancy, $0 \leq \theta_T \leq 1$. Accordingly, the lattice and trap hydrogen concentrations can be defined as $C_L = \theta_L N_L$ and $C_T^i = \theta_T^i N_T^i$, and the hydrogen transport equation can be written as,

$$\frac{\partial \theta_L}{\partial t} + \sum_{i=1}^{n_t} \frac{N_T^{(i)}}{N_L} \frac{\partial \theta_T^i}{\partial t} = D_L \frac{\partial^2 \theta_L}{\partial x^2} \quad (4)$$

The rate of trapped hydrogen, the $\partial \theta_T / \partial t$ term in Eq. (4), can be defined using the trapping and de-trapping rates, using the McNabb-Foster model, or directly linked to the lattice concentration by assuming equilibrium through the Oriani model. Here, and in our machine-learning approach, we will consider both.

2.1.1. McNabb-Foster model

The McNabb-Foster model [38] accounts for trapping kinetics and, in combination with Eq. (4), for the role of hydrogen diffusion. The framework assumes the presence of sparsely distributed and isolated traps, thus negating the possibility of any trap interaction from occurring. For hydrogen to transition from one trap site to another, it must pass through an intermediate lattice site. Modelling of the trapping and de-trapping kinetics of the hydrogen atoms is based on the energy landscape for the diffusion of hydrogen in metals (Fig. 2). The net rate of trapped hydrogen concentration is described as:

$$\frac{\partial \theta_T^{(i)}}{\partial t} = k^{(i)} \theta_L (1 - \theta_T^{(i)}) - p^{(i)} \theta_T^{(i)} (1 - \theta_L^{(i)}) \quad (5)$$

where k and p are the rates of hydrogen migrating from a NILS to a trap site and vice versa. They are defined as:

$$k^{(i)} = v_t^{(i)} \exp\left(-\frac{E_t^{(i)}}{RT}\right) \quad (6)$$

$$p^{(i)} = v_d^{(i)} \exp\left(-\frac{E_d^{(i)}}{RT}\right) \quad (7)$$

where $v_t^{(i)}$ and $v_d^{(i)}$ are the pre-exponential factors for trapping and de-trapping, respectively, and $E_t^{(i)}$ and $E_d^{(i)}$ are the trapping and de-trapping energies.

2.1.2. Oriani's model

The McNabb-Foster framework can be simplified by assuming local equilibrium between trap and lattice sites, as demonstrated by Oriani [39]. This assumption allows us to use the trap kinetic differential equation, Eq. (5), by assuming equilibrium to directly relate the trapped and lattice hydrogen:

$$\frac{\theta_T^{(i)}}{1 - \theta_T^{(i)}} = \frac{\theta_L}{1 - \theta_L} K_T^{(i)} \quad (8)$$

where K_T is the equilibrium constant, which is given by

$$K_T^{(i)} = \frac{k^{(i)}}{p^{(i)}} = \frac{v_t^{(i)}}{v_d^{(i)}} \exp\left(\frac{-\Delta H^{(i)}}{RT}\right) \quad (9)$$

with the binding energy being equal to the difference in trapping and de-trapping energies, $\Delta H^{(i)} = E_t^{(i)} - E_d^{(i)}$. As a result, Eq. (4) can be reduced to a single second-order PDE solely dependent on θ_L :

$$\frac{\partial \theta_L}{\partial t} \left(1 + \sum_i \frac{N_T^{(i)} K_T^{(i)}}{N_L [1 + (K_T^{(i)} - 1) \theta_L]^2} \right) + \sum_i \frac{N_T^{(i)} K_T^{(i)} \Delta H^{(i)} \phi(\theta_L - \theta_L^2)}{N_L [1 + (K_T^{(i)} - 1) \theta_L]^2} = D_L \frac{\partial^2 \theta_L}{\partial x^2} \quad (10)$$

Both the Oriani and McNabb-Foster models typically provide the same results [61]. This is further investigated in Section 2.3.2, where it is shown that both models deliver the same result for relevant values of the vibration frequency. Oriani's model does not require solving for the trap density explicitly, halving the number of degrees of freedom. On the other hand, McNabb-Foster's relations bring a reduced nonlinearity, making them easier to solve. Both approaches are considered here, although the experimental case studies will only make use of the McNabb-Foster formulation for simplicity, considering a vibration frequency equal to the Debye frequency ($\nu = 10^{13}$ Hz), which delivers results identical to those obtained with Oriani's model (see Section 2.3.2).

2.1.3. Initial and boundary conditions

On the left and right edges of the TDS specimen, interstitial lattice hydrogen is able to desorb from the sample, as shown in Fig. 1(a). At equilibrium, the occupancy of hydrogen at these boundaries can be determined based on the exterior hydrogen pressure through Sievert's Law:

$$\theta_L = \frac{S}{N_L} \sqrt{p_{H_2}} \quad (11)$$

with the solubility S depending on the temperature through an Arrhenius law. Here, we will idealise this to assume a full vacuum around the TDS sample (any hydrogen that diffuses outside of the metal is removed instantly), such that our boundary conditions can be simplified to $\theta_L = 0$. This is representative of modern ultra-high-vacuum TDS equipment. To enforce this and obtain the hydrogen flux, the boundary flux (per unit area) is defined through a penalty-based approach,

$$j = -D_L \frac{\partial C_L}{\partial x} \Big|_{x=L/2} = k \theta_L \exp \left(\frac{-E_{bc}}{RT} \right) \quad (12)$$

where the penalty factor k is chosen to be high enough to enforce this boundary condition. A value of $k = 8 \times 10^5$ mol/m²/s is chosen here, as it is much higher than the diffusivity, thus ensuring the boundary condition will always be fulfilled. The exponential term, with the variable $E_{bc} = 1.71 \times 10^4$ J/mol, allows this penalty factor to scale as the temperature increases, such that the penalty factor always remains large compared to the diffusion and de-trapping rates. The appropriateness of the selected values of k and E_{bc} in the computational model was evaluated in Section 2.3.1. The use of a penalty-based boundary condition, relative to a conventional Dirichlet one ($\theta_L = 0$), enables a more precise determination of the hydrogen flux, allowing for the use of coarser meshes and thus accelerating the training stage. The relation described in Eq. (12) follows that of the Tafel reaction for hydrogen desorption, in which case the constants k and E_{bc} have the physical meaning of reaction rate and energy, respectively. Hence, the kinetics of surface reactions [62,63] can be accounted for in the present model. However, it should be noted that we have solely used this relation as a way to enforce a zero hydrogen boundary condition; it does not account for any surface reaction kinetics, which are assumed to be negligible, given that they occur at much faster rates than the bulk processes taking place. The effect of this boundary condition was verified by increasing and decreasing k by a factor of ten, which did not alter the obtained results.

To mirror the TDS experimental process, the simulation has been divided into three sequential steps: (i) hydrogen charging of the sample, (ii) rest period, representing the transfer from the charging step to the TDS apparatus, and (iii) TDS testing at a fixed heating rate. While the charging process can be simulated within the present framework, it is common practice to charge the sample until saturation; i.e., until a uniform occupancy $\theta_L(x, t = 0) = \theta_L^0$ is reached throughout the sample. Accordingly, this is the initial condition in our simulations. When using the Oriani model, this automatically adapts the trapped hydrogen contents to be in equilibrium with this initial concentration. In contrast, when using the McNabb-Foster model, the trapped hydrogen is initialised assuming equilibrium between the trapped and lattice concentrations, via:

$$\theta_T^{(i)0} = \frac{\theta_L K_T^{(i)}}{1 + (K_T^{(i)} - 1) \theta_L} \quad (13)$$

with $K_T^{(i)}$ given by Eq. (9).

2.2. Numerical implementation

Both the McNabb-Foster and Oriani frameworks were implemented in the computational model. The coupled PDEs of the McNabb-Foster formulation and the single second-order PDE of Oriani's theory are numerically solved in one-dimensional form using the finite element method, which was programmed in Python. Linear elements were used to discretise the domain, such that the hydrogen concentration is given by:

$$C_L = \mathbf{N} \mathbf{c}_L \quad (14)$$

with the vector \mathbf{N} containing the shape functions, and the vector \mathbf{c}_L the nodal values for the hydrogen concentration. As the domain is symmetric, we are only solving for half the domain. To ensure stability of the simulations, a backward Euler time discretisation scheme was used. As a result, the discretised weak form for the lattice hydrogen is given by:

$$\int_{\Omega} \mathbf{N}^T \mathbf{N} \frac{\mathbf{c}_L^{t+\Delta t} - \mathbf{c}_L^t}{\Delta t} + D_L \nabla \mathbf{N}^T \nabla \mathbf{N} \mathbf{c}_L^{t+\Delta t} + \mathbf{N}^T J_{\text{traps}} \, d\Omega + \int_{\Gamma} \frac{k}{N_L} \exp \left(\frac{-E_{bc}}{RT} \right) \mathbf{N}^T \mathbf{N} \mathbf{c}_L \, d\Gamma = 0 \quad (15)$$

where the interior of the domain is denoted by Ω , and the edge by Γ . For the Oriani model, the trapping-related fluxes are obtained as:

$$J_{\text{traps}} = \sum_i \frac{N_T^{(i)} K_T^{(i)}}{N_L [1 + (K_T^{(i)} - 1) \mathbf{N} \mathbf{c}_L^{t+\Delta t} / N_L]^2} \mathbf{N} \frac{\mathbf{c}_L^{t+\Delta t} - \mathbf{c}_L^t}{\Delta t} + \frac{N_T^{(i)} K_T^{(i)} \Delta E^{(i)} \phi(\mathbf{N} \mathbf{c}_L^{t+\Delta t} / N_L - (\mathbf{N} \mathbf{c}_L^{t+\Delta t} / N_L)^2)}{N_L (1 + (K_T^{(i)} - 1) \mathbf{N} \mathbf{c}_L^{t+\Delta t} / N_L)^2} \quad (16)$$

In contrast, if using the McNabb-Foster model, the trapping-related flux is given by:

$$J_{\text{traps}} = \frac{1}{N_L} \sum_i J_{\text{trap}}^{(i)} \quad (17)$$

$$J_{\text{trap}}^{(i)} = N_T^{(i)} \left(k^{(i)} \frac{\mathbf{N} \mathbf{c}_L^{t+\Delta t}}{N_L} \left(1 - \frac{\mathbf{N} \mathbf{c}_T^{(i)t+\Delta t}}{N_T} \right) - p^{(i)} \frac{\mathbf{N} \mathbf{c}_T^{(i)t+\Delta t}}{N_T} \left(\frac{\mathbf{N} \mathbf{c}_L^{t+\Delta t}}{N_L} \right) \right) \quad (18)$$

Finally, for the McNabb-Foster model, this is supplemented with the discretised weak forms for the trapped hydrogen concentration:

$$\int_{\Omega} \mathbf{N}^T \mathbf{N} \frac{\mathbf{c}_T^{(i)t+\Delta t} - \mathbf{c}_T^{(i)t}}{\Delta t} - J_{\text{trap}}^{(i)} \, d\Omega = 0 \quad (19)$$

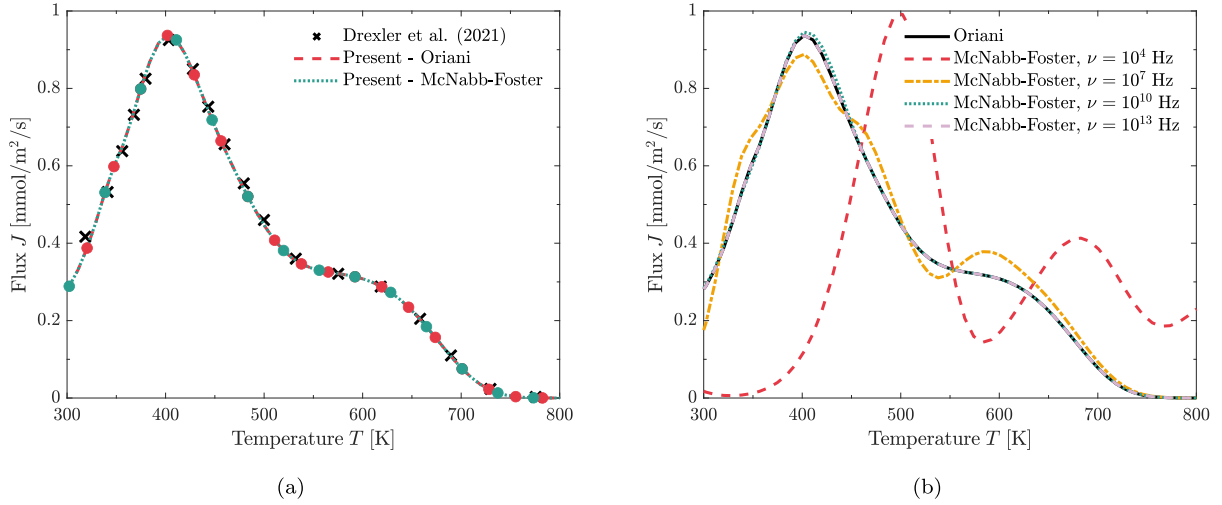


Fig. 3. Validation of the Oriani and McNabb-Foster implementations for multi-trap systems: (a) comparison between the desorption spectrum reported by Drexler et al. [41] and that obtained with the developed computational model, (b) comparison of TDS simulations considering the McNabb-Foster formulation for different values of jump frequency ($\nu_t = \nu_d = \nu$) and Oriani's model.

These equations are solved using a Newton–Raphson-type algorithm. To ensure stability for the McNabb-Foster scheme, even for high values of the jump frequency ν , a lumped integration scheme is used for the trapping terms [64].

The boundary value problem is effectively one-dimensional as the TDS sample thickness L is much smaller than the other dimensions. Also, symmetry conditions apply. Therefore, we consider a 1D bar of length $L/2$ with appropriate symmetry conditions, $\partial C_L/\partial x = 0$ at $x = 0$. A uniform mesh with 25 elements is used to discretise the sample. This discretisation is sufficient to achieve mesh-independent results within the present scheme. The time increment was selected as large as possible without losing accuracy.

It should be noted that, while demonstrated with the two most widely used hydrogen transport/trapping models (McNabb-Foster, Oriani), the present ML-based framework can be applied to other modelling strategies, allowing it to encompass other physical phenomena that are not embedded in conventional hydrogen transport and trapping models, such as dislocation-mediation transport [65,66] or trap interconnectivity [67–69].

2.3. Model verification

A thorough validation of the developed computational model is conducted in this section. Each of the elements of the implemented formulation are verified. Firstly, the implementation of each hydrogen transport theory is assessed. The spectra obtained with both McNabb-Foster's and Oriani's models for multi-trap systems are compared with the numerical results obtained by Drexler et al. [41]. Subsequently, the agreement between the McNabb-Foster and Oriani theories is assessed. Different values of trapping and de-trapping frequencies are evaluated to understand the regime of validity of Oriani's equilibrium assumption. Finally, the impact of sample frequency on the convergence of the solution is assessed.

2.3.1. Multi-trap system

The implementation of both hydrogen transport frameworks for multi-trap systems was validated by comparing the predictions of the developed numerical model against results obtained by Drexler et al. [41], who used Oriani's method and the finite differences approach. Given that Drexler et al. [41] adopted Oriani's method throughout their study, a high jump frequency, equal to the Debye frequency ($\nu = 10^{13}$ Hz), was selected for the McNabb-Foster implementation to

ensure the system is within the equilibrium regime, and thus comparable to Oriani's method (see Section 2.3.2). Finally, the penalty factor k and variable E_{BC} were fixed at 8×10^5 mol/m²/s and 1.71×10^4 J/mol, respectively. The results, reported in Fig. 3(a), show clear agreement between both frameworks and the reference results, confirming the correct implementation of the computational schemes and the effective enforcement of the penalty-based approach by the selected values of k and E_{BC} . We have further verified that these values for k are sufficiently high to enforce this boundary condition by simulating the same case with $k = k/10$, which produced identical results.

2.3.2. McNabb-Foster vs. Oriani models

To assess the agreement between the McNabb-Foster and Oriani formulations, simulations for the same multi-trap system are carried out using these two models. Four McNabb-Foster simulations are run with increasing values of jump frequency to determine the value required for the McNabb-Foster model to converge to Oriani's model, and thus understand the validity regime of the equilibrium assumption adopted in the latter. To conduct this analysis, the multi-trap system constructed by Drexler et al. [41], previously considered in the multi-trap system validation study (Section 2.3.1), is selected. The results, depicted in Fig. 3(b), indicate that convergence occurs for sufficiently high values of jump frequency ν . A good agreement is obtained between the Oriani and McNabb-Foster predictions for values equal to or larger than $\nu = 10^{10}$, and a perfect alignment between the two models is achieved at $\nu = 10^{13}$, also referred to as the Debye frequency. In the remainder of the report, the McNabb-Foster model will be implemented with a frequency that matches the Debye frequency. This choice ensures that the system remains within the equilibrium regime of validity, which will help facilitate comparisons.

2.3.3. Time step convergence study

A time step convergence study was conducted for both McNabb-Foster and Oriani frameworks. Simulations of the multi-trap system constructed by Drexler et al. [41] were carried out for increasing values of sample frequencies, $f = 1, 3, 5, 10, 20, 50, 100$, and compared to the original data simulated by the authors. The number of temperature evaluations that are saved as the output TDS curve was fixed at $n_{tp} = 64$, thus the time steps corresponding to the evaluated frequencies are $\Delta t = 4.5, 1.5, 0.91, 0.45, 0.23, 0.091, 0.045$ s.

Convergence is achieved for both McNabb-Foster and Oriani frameworks at $f = 10$, $\Delta t = 0.45$ s; consequently, this value was selected for all validation studies (Fig. 4). Convergence studies were repeated for each simulated and experimental dataset, and similar results were obtained.

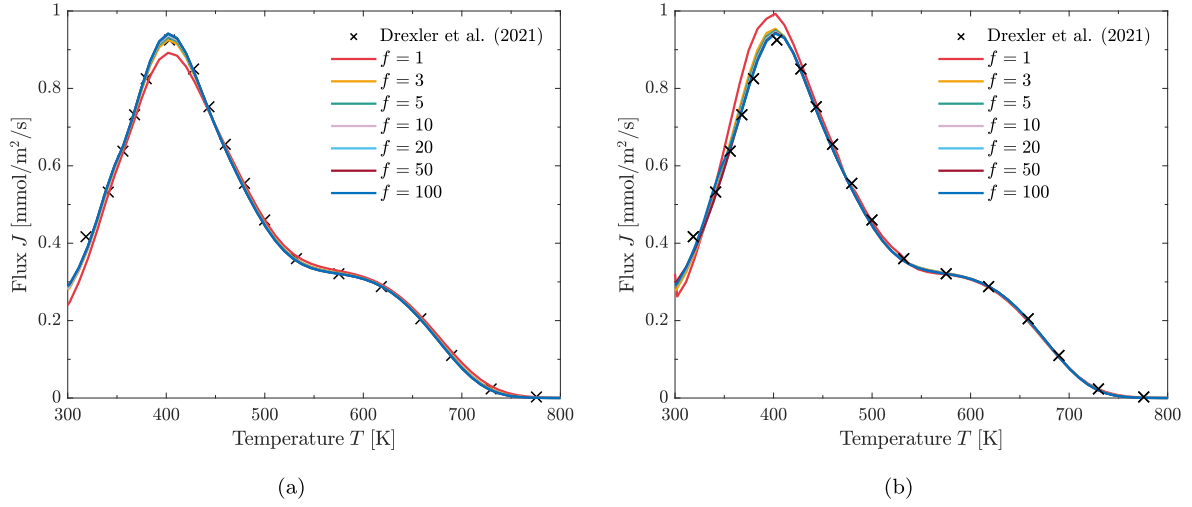
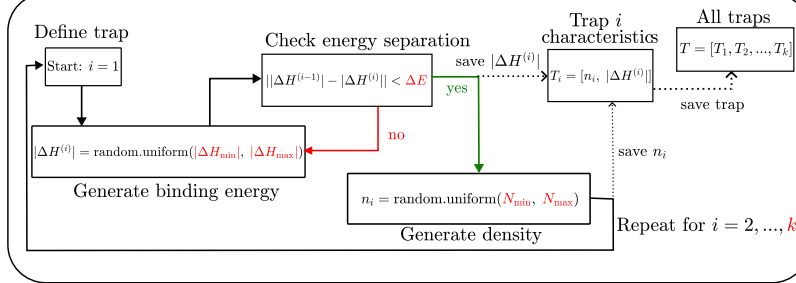


Fig. 4. Sample frequency (and time step) convergence study for (a) McNabb-Foster and (b) Oriani framework implementations. The TDS simulation predictions obtained using different sample frequencies are benchmarked against the multi-trap system simulated by Drexler et al. [41].

1. Parameter Selection

- (a) Number of traps in sample: k
- (b) Trapping energy: fixed at E_L kJ/mol
- (c) Range of allowable absolute binding energies: $|\Delta H_{\min}|$ to $|\Delta H_{\max}|$ kJ/mol
- (d) Minimum difference between binding energies: ΔE kJ/mol
- (e) Range of allowable trap densities: N_{\min} to N_{\max} sites/m³

2. Trap Generation



3. TDS Simulator

- (a) Define sample: material, traps
- (b) Define initial lattice hydrogen concentration
- (c) Rest
- (d) Perform TDS test

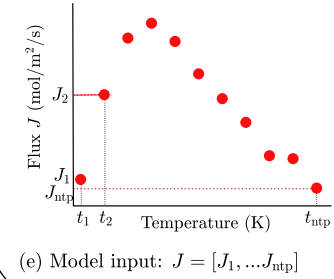


Fig. 5. Schematic of the procedure used to generate a single data point corresponding to a TDS sample with k distinct traps. The process comprises three phases: (1) selection of parameters, (2) generation of trap characteristics, and (3) TDS simulation to produce the desorption spectrum.

2.4. Data generation

To train our multi-NN model, datasets need to be generated based on simulated data. A dataset consists of n data points, with each data point representing a sample. Each data point contains information on the trapping characteristics of the sample, including the number of traps, and the associated densities and binding energies. Additionally, each data point includes the temperatures and fluxes that constitute the desorption spectrum of that specific sample.

Each data point in the dataset is generated through a systematic procedure that is divided into three distinct phases. Firstly, the parameters guiding the data generation are selected. This includes the maximum number of (potential) trap types in the sample, the range of allowable trap densities, the trapping energy (fixed as the activation energy for lattice diffusion E_L for all traps, as commonly done in the literature [70]), the range of allowable absolute binding energies, and the minimum allowable separation between the binding energies of traps in the same sample. Based on these parameters, the trapping characteristics of the sample are generated. The detailed procedure is illustrated in Fig. 5. For each trap, the trapping energy is set to E_L , and

the absolute binding energy is assigned a value randomly selected from the allowable range. Subsequently, the difference in the absolute binding energy of the newly generated trap and the previously generated traps in the sample is evaluated to ensure all traps are slightly distinct. If the difference is less than the minimum allowable separation, the binding energy generation step is repeated until a suitable value is found. The trap is then assigned a density, randomly chosen from the permissible range, and its characteristics are stored alongside those of the other traps. To ensure each TDS spectrum corresponds to a unique set of trapping energies, these traps are ordered from lowest to highest energy. This uniqueness is required for the ANN to be able to relate TDS curves to trap characteristics.

A critical step in the first two phases of the data generation process is defining the range of allowable trap densities and binding energies that encompass all possible trap configurations that could contribute to the TDS spectrum under consideration. Trap densities and absolute binding energies can vary significantly. Shallow traps can have absolute binding energies $|\Delta H| < 30$ kJ/mol while the binding energies of deep traps can be $|\Delta H| > 60$ kJ/mol. Large differences in N_T and $|\Delta H|$ make it challenging to cover the entire trap domain effectively

using the random generation approach. Thus, for each test case, it is essential to identify the regime of interest—based on observed flux magnitudes and peak temperatures of the TDS spectrum—to simplify the data generation process and ensure that only relevant spectra are considered for model training.

In the final phase, the simulation of the TDS experiment is carried out. This requires several additional material, test, and numerical parameters that characterise the experimental TDS procedure and material used. The material parameters consist of the pre-exponential diffusion coefficient D_0 , initial lattice hydrogen concentration C_0 , density of interstitial lattice sites N_L , and activation energy for lattice diffusion E_L . If the McNabb-Foster framework is employed, the vibration frequency is also required. This is set equal to the Debye frequency ($\nu = 10^{13}$ Hz), as this is its expected magnitude [43]. The required test parameters are: sample thickness L , rest time t_{rest} , heating rate ϕ , and minimum T_{min} and maximum T_{max} temperatures. For the numerical parameter inputs, one only needs the number of temperature evaluations (ntp), which defines how many desorption flux values are recorded, and the sampling frequency (f), which specifies the number of time steps between each recorded value. The TDS test time t_{test} can be estimated using $t_{\text{test}} = (T_{\text{max}} - T_{\text{min}})/\phi$. The time increment can then be calculated using $\Delta t = t_{\text{test}}/(ntp \times f)$. The frequency enables us to reduce the number of temperature evaluations that are saved without increasing the time increment, ensuring stability is achieved for all cases while allowing the number of inputs for the ANN to still be reasonable.

3. Machine learning approach

The multi-NN model proposed for the quantitative analysis of TDS spectra comprises two multi-layer, fully connected, feed-forward NNs trained with back-propagation [71–73]. The detailed structure and flowchart of the multi-NN model are illustrated in Fig. 6. The first step involves passing the input data to the first NN, referred to as the classification model, which predicts the number of traps present in the material. An intermediate stage follows, in which the appropriate second NN, the regression model, is selected. This model is trained to predict trapping properties based on the number of traps, allowing the appropriate model to be chosen based on the classification model's prediction. Finally, the input data is fed into the regression model, which computes the densities and absolute binding energies. Both neural network models are implemented using the Keras machine-learning framework [74,75]. In this section, we will first describe the optimised structure of the ANN models, after which we will briefly discuss the parameter and re/post-processing procedure tuning that has been performed to reach this optimised architecture.

3.1. Optimised multi-model neural network architecture

The input vector for both neural networks consists of hydrogen desorption rate data from the thermal desorption spectra; specifically, 64 flux values sampled at evenly spaced temperature intervals. To enhance convergence and stability, a minimum threshold of 10^{-10} mol/(m² s) is applied to all flux values. Additionally, due to the significant differences in magnitude among the fluxes, a log transformation is applied to the input data, resulting in the following calculation for each flux value:

$$J_{\text{input}}^n = \log(\max(J^n, 10^{-10})) \quad (20)$$

No normalisation is performed beforehand, as the Keras-provided normalisation layer is added after the input layer in both networks, eliminating the need for pre-processing of this type. This layer applies z-score standardisation, scaling the (log-scaled) input fluxes based on the average and standard deviation of the training dataset. The effect of this scaling is demonstrated in Section 3.3.

3.1.1. Hidden layers

As the input vector size is 64, the input layer for both NNs comprises 64 neurons. These inputs are passed onto the different layers, which differ between the NNs. The hidden layer topology of the regression model can be summarised as 64-64-32-16-8, all multiplied by the number of outputs, e.g., 256-256-128-64-32 for predicting the energies and densities for a two-trap system. The choice to scale the number of nodes in the hidden layers with the number of outputs of the NNs was made to account for the increase in complexity associated with the increase in the number of traps. In the classification model, the hidden layers are structured as 256-128-64-32. The rectified linear (ReLU) activation function is used throughout the layers [73].

3.1.2. Post-processing

The two models also differ in their post-processing procedures. In the classification model, the softmax activation function is used in the output layer to convert the output values into discrete probabilities (see Fig. 6). The maximum probability is then taken as the prediction for the number of trapping sites. In the regression model, the output vector is divided into two vectors: values corresponding to trap energies (positions 1 to ntp) and densities ($ntp + 1$ to $2 \times ntp$). Each vector is passed through its respective inverse transform scaler to recover the actual (unscaled) absolute binding energy and density values, which are then recombined into a single output vector. Separate scalers are used for absolute binding energies and densities due to their significantly different magnitudes—energies are typically 2 to 3 orders of magnitude greater than densities. When a single combined scaler was used, it was observed that the larger energy values dominated the scaling process, adversely affecting the learning of density values. This imbalance led to significantly higher prediction errors in the density outputs, justifying the use of two independent scalers.

3.1.3. Model training

Training is achieved by employing the supervised learning process, which intends to map input examples of TDS data to a known number of traps and densities/energies for the classification and regression models. Prior to training the model, the training datasets must be generated. In addition to the data generation parameters specified in Section 2.4, we also define the maximum number of traps that the multi-NN model is expected to predict. The total number of datasets generated corresponds to this maximum value. For instance, if the maximum number of traps is set to 4, four distinct datasets are created. Each dataset contains data points representing TDS samples with a distinct number of traps, ranging from 1 in the first dataset to the maximum (4) in the final dataset. The data points of each dataset are generated following the procedure outlined in Fig. 5, with the number of traps k set to the specific number of traps for that dataset. Each dataset is subsequently used to train a regression model corresponding to the number of traps of the respective dataset. Finally, the classification model is trained using the combined set of all datasets.

All ML models were trained with a dataset comprising 50,000 data points (i.e., simulations). To evaluate the NN model's performance during training, the database of simulation results was split into training and validation sets, using an 80/20 split. An additional test set comprising 500 data points was generated to evaluate the final model. Given that the training data is synthetic and thus unlimited datasets can be generated, the simple hold-out validation approach is adopted, which is appropriate for this purpose [72].

The training process uses the same optimiser for both models, Adamax, due to its stability and efficiency in training deep networks, with learning rate and weight decay set to 10^{-3} [73]. The choice of loss function, however, is task-dependent [72,76]. For the regression model, we use Mean Squared Error (MSE):

$$\text{MSE} = \frac{1}{n} \sum_{i=1}^n (j_i - j_i')^2 \quad (21)$$

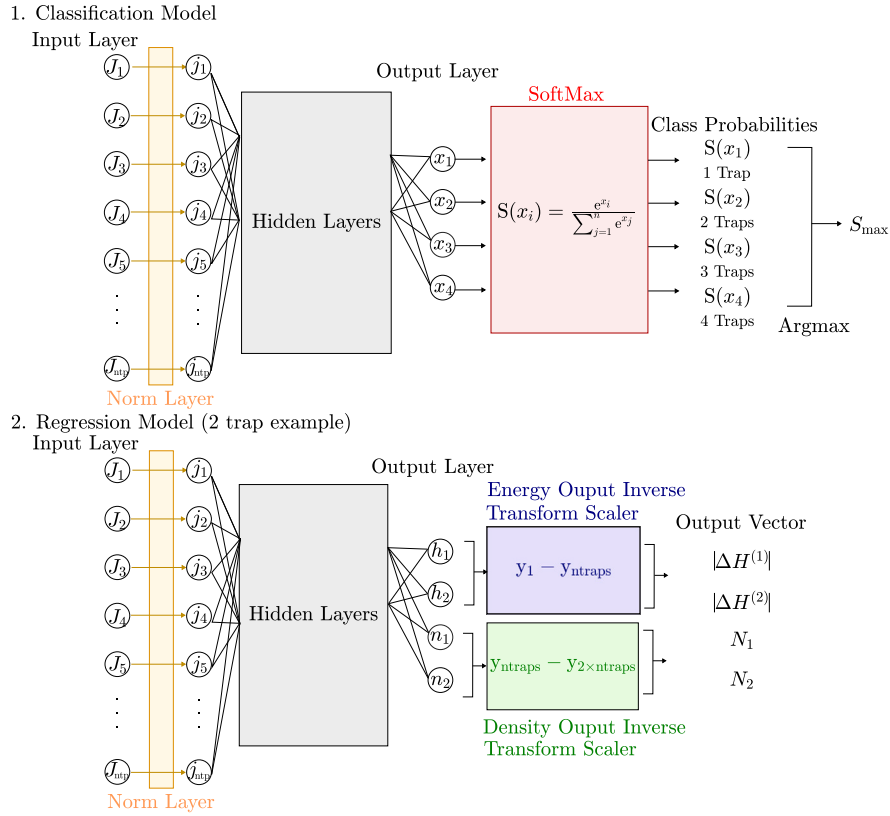


Fig. 6. Overview of the NN-coupled TDS-based analysis framework for characterising hydrogen trapping parameters. Two multi-layer, fully connected, feed-forward NNs are employed. The first NN, a classification model, extracts the number of traps present in the sample. The second NN, a regression model, predicts the binding energies and densities of each trap. The variables in the regression model's output vector, e_i and n_i , represent the scaled absolute binding energy and density of trap i , respectively. These scaled parameters are transformed back to their original units and scale, $|\Delta H^{(i)}|$ and N_T^i , by applying the appropriate inverse scaler.

where n is the number of predictions, J_i is the true output (i.e., simulation results), and J'_i is the predicted output from the neural network. MSE is well-suited for regression-type problems because it heavily penalises larger errors, encouraging precise, continuous-value predictions [58]. However, MSE is inappropriate for classification tasks, as it assumes a continuous output and fails to model class probabilities effectively. For classification, we instead use cross-entropy loss:

$$\text{cross-entropy loss} = - \sum_{i=1}^n \sum_{k=1}^m J_{ik} \ln J'_{ik} \quad (22)$$

where m is the number of output nodes in the neural network. When the number of output layer nodes matches the number of classes (as in our model), cross-entropy corresponds to the negative log-likelihood of the observations. Thus, the loss function penalises confident but incorrect predictions, making it ideal for classification tasks by encouraging accurate probability distributions [73]. The batch size was fixed at 32 for both models. The number of training epochs was set to 100 and 200, multiplied by the number of outputs, for the classification and regression models, respectively.

3.2. Model optimisation: hyperparameter tuning

The hyperparameter tuning process consists of identifying the combination of hyperparameters that optimises the efficiency, performance, and generalisation of the models [72]. This ensures that it provides the best possible predictions given a fixed amount of training data, reducing the computational cost of both the data generation and the training process. The optimal set of hyperparameters is highly dependent on factors such as the nature of the inputs (i.e. data distribution, dimensionality and quality), the outputs, and the complexity of the task. Since these factors vary significantly across the regression and

classification ANNs, the hyperparameter tuning process was repeated for each model individually to account for these differences.

For each NN, the hyperparameter tuning process followed a systematic approach, divided into three sequential stages. Each stage focused on optimising a different category of hyperparameters: architecture, algorithm, and regularisation hyperparameters. During the entire tuning process, several hyperparameters were kept constant: the number of training epochs ($100 \times$ number of outputs), the batch size (32), and the number of training data points (10,000). The hyperparameter tuning is performed on a lower amount of training data compared to the actual model training, to allow a large range of hyperparameter combinations to be explored. However, it is expected that the parameters optimised here will still be (close to) optimised for larger amounts of training data.

3.2.1. Model architecture

The first stage involved optimising the model architecture by tuning key hyperparameters—specifically, the number of hidden layers and the number of nodes per layer. Recommendations exist in literature on how to approach this process [77–79]. In this work, the network topology was chosen by systematically varying the architecture while monitoring model performance. For the regression models, we evaluated three levels of complexities (i.e., 128-64, 64-64 and 128-128) defined by the number of nodes in the first two hidden layers. Subsequent layers decreased progressively in size; for instance, in a 128-64 topology, the third layer has 32 nodes, the fourth layer 16 nodes, and so forth. The number of nodes in each hidden layer is scaled by a factor proportional to the number of model outputs, allowing complexity to increase with output dimensionality. For each complexity, topologies of four to seven hidden layers were tested. A similar analysis was conducted for the classification model, with five levels of complexity

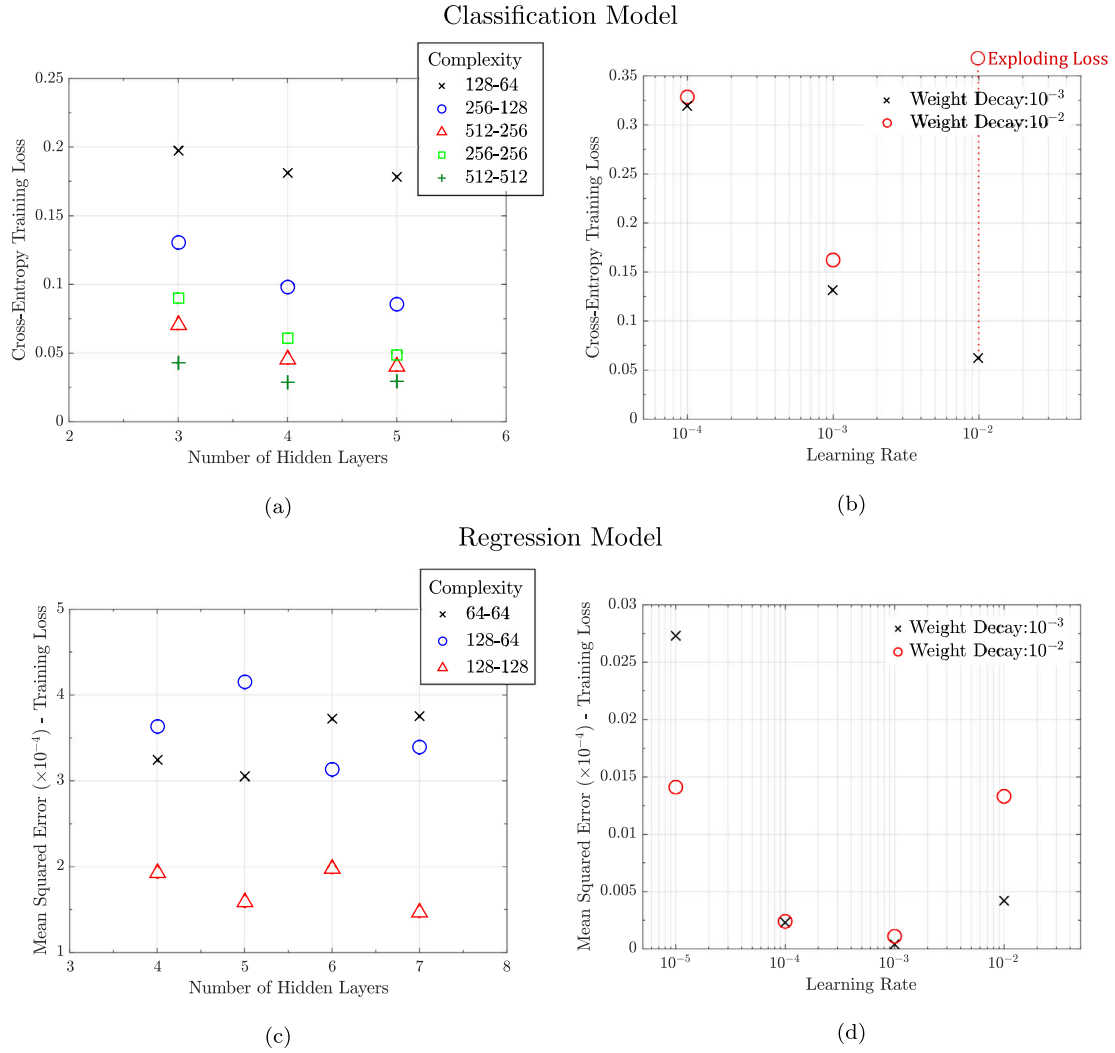


Fig. 7. Hyperparameter tuning results for (a, b) classification and (c, d) regression models. Subfigures (a) and (c) show the effect of the number of hidden layers on training loss for various model complexities. Complexity is defined by the number of nodes in the first two hidden layers, with subsequent layers halving in size (e.g., a 128-64 topology continues with 32, then 16 nodes). Subfigures (b) and (d) show how training loss varies with the learning rate (Adamax optimiser), evaluated at two weight decay values: 10^{-2} and 10^{-3} .

(i.e., 128-64, 256-128, 512-256, 256-256, 128-128) and topologies ranging from three to five hidden layers. The scaling factor in this case was the maximum number of output classes (i.e., maximum potential traps). Throughout the analysis, certain hyperparameters were held constant: the Adamax optimiser was used with a learning rate and weight decay of 10^{-3} , and ReLU was applied as the activation function in all hidden layers.

The results are shown in Figs. 7(c) and 7(a) for regression and classification models, respectively. For the regression model, increasing the number of layers or nodes did not significantly reduce the training loss, which remained between 1.5×10^{-4} to 4.5×10^{-4} . Thus, a simple topology comprising five hidden layers (i.e., 64-64-32-16-8) was chosen to minimise computational cost. In contrast, the classification model benefited from increased complexity. For instance, in three-layer topologies, increasing the number of nodes in the first two hidden layers from 128-64 to 512-256 reduced the training loss by more than 0.1 (see Fig. 7(a)). However, the benefit of adding more layers diminishes: for each level of complexity, the training loss with five layers is nearly identical to that with four (see Fig. 7(a)). A topology of medium complexity comprising 4 hidden layers (i.e., 256-128-64-32) was selected. More complex topologies were not considered, as mitigating over-fitting in such models would require significantly more

training data, increasing both data generation and model training computational costs.

3.2.2. Algorithmic hyperparameters

With regards to the algorithm hyperparameter stage, different combinations of learning rate and weight decay were investigated. Keras Tuner [75] was used to conduct a grid search tuning study. The values of learning rate and weight decay investigated were $[10^{-5}, 10^{-4}, 10^{-3}, 10^{-2}]$ and $[10^{-3}, 10^{-2}]$ respectively. The optimised topologies were selected to conduct the study. The results obtained for the classification and regression models are reported in Figs. 7(b) and 7(d), respectively. For both NNs, a learning rate and weight decay of 10^{-3} is required to achieve optimal performance.

3.2.3. Regularisation

A preliminary study was performed to evaluate the suitability of the most commonly used regularisation techniques for mitigating over-fitting, specifically penalty-based regularisation and dropout layers. Dropout layers were incorporated after each hidden layer, with dropout rates of 0.2, 0.3, and 0.5 tested. For penalty-based regularisation, L2 regularisation was assessed with values ranging from 10^{-3} to 10^{-1} , applied exclusively to the hidden layers. The inclusion of these techniques did reduce over-fitting; however, it also led to a degradation

in model performance. This trade-off renders regularisation ineffective in improving overall model performance. Consequently, regularisation techniques were not integrated into the final model. The most effective approach to mitigating over-fitting identified in this study was to increase the number of training data points.

3.3. Model optimisation: data pre-processing

A major challenge in applying ANN to TDS curves arises from the fact that both input and output parameters span several orders of magnitude. Conventional ML schemes assume the inputs and outputs to be linearly spaced, as is the case for the trapping energy. These energies are typically between 10–100 kJ/mol [48,80], with errors in the estimates of these energies being equal throughout this range, e.g. a difference of ± 5 kJ/mol has the same effect whether it is 50 ± 5 or 150 ± 5 kJ/mol. This energy relates to the horizontal location of the peaks within a TDS curve in a (mostly) linear manner, making it a fairly easy quantity for ANN to predict. In contrast, trapping densities span many orders of magnitude, e.g., ranging from 10^{23} to 10^{28} sites/m³ [81,82]. Using these densities directly in the NN would result in bias, as the network would favour accurately predicting the higher densities, which contribute to the largest mean squared error (MSE). To ensure the prediction error scales with the predicted quantity, a pre-processing algorithm is applied to transform the density into a linear scale.

To achieve this, different combinations of transformation and scaling techniques were applied to the input data features and output predictions with the objective of adjusting the distributions to more closely resemble a normal distribution. For the input data (the TDS curves), Log and Yeo-Johnson power transformations [83] were used to reduce the skewness and kurtosis of each feature's distribution. Both transformations achieved similar effects; however, the log transformation was selected due to its lower computational cost.

Following the transformation, normalisation techniques were applied. Both min–max scaling and z-score scaling were assessed after applying the log transformation. Models trained with log-transformed and z-score-scaled data achieved a lower mean absolute error (MAE), leading to the selection of z-score scaling as the optimal normalisation technique. While normalisation techniques do not impact the skewness or kurtosis, the mean and standard deviation were checked to confirm successful scaling, with values approximately equal to 0 and 1 for all features.

The impact of each stage of the optimised pre-processing technique on the distribution of eight input features is depicted in Fig. 8. The selected features are evenly distributed across the temperature range, representing the entire feature set. The raw data is highly skewed and deviates significantly from a normal distribution (Fig. 8(a)). After applying the log transformation (Fig. 8(b)), there is a significant reduction in skewness. Notably, the skewness of feature 8, which initially exhibited the highest skewness, decreased from 3.4 to 0.2. With the addition of z-score scaling (Fig. 8(c)), the distribution of all features more closely resembles a normal distribution, having a mean and a standard deviation approximately equal to 0 and 1, respectively. Despite the transformations, several outliers remain, likely due to the highly skewed nature of the raw data, as observed in Fig. 8(c). To further improve the distributions, a threshold of 10^{-10} was applied to all flux values to clip very small values before applying the transformation and normalisation techniques.

Finally, zero-mean Gaussian noise was introduced into the training data. This step is essential for accurately fitting experimental data, as the synthetic training data is noise-free, while real-world data is inherently noisy. The first case study was used to determine the appropriate level of noise, with three noise levels tested—corresponding to standard deviations of 0.01, 0.05, and 0.1, representing increasing intensity. The optimal noise level was identified as that corresponding to a standard deviation of 0.05. The analysis was repeated for the second and third case studies to verify consistency across scenarios.

4. Parameter identification of experimental TDS data

To demonstrate the ability of ML models to determine the trapping characteristics—number of trapping defects, trap binding energies and trap densities—from experimental TDS spectra, three test cases were analysed corresponding to: (1) a high-strength AISI 4340 tempered martensitic steel; (2) a tempered martensitic Fe-C-Ti alloy, containing 0.1 wt% C and a stoichiometric amount of Ti; and (3) a tempered martensitic Fe-0.05C-0.20Ti-2.0Ni alloy. For each test case, the experimental TDS spectra were fitted using the NN procedure outlined in Section 3. To evaluate the accuracy and reliability of the developed ML models, an analysis of each TDS spectrum was also carried out using an already established approach—applying the inference fitting capabilities embedded in the TDS Simulator App described by Garcia-Macias et al. [43]. This fitting is based on the particle swarm optimisation (PSO) algorithm implemented in MATLAB. Throughout the remainder of the paper, we refer to the fitting of experimental data using the TDS Simulator App [43] as the ‘conventional optimisation’ approach, which serves as a reference to assess the accuracy of our machine-learning-based approach against conventional optimisation schemes. For each test case, the test and material parameters were kept consistent across both the conventional and the ML analyses to ensure that the results were directly comparable.

4.1. High-strength AISI 4340 tempered martensitic steel

The first test case involves three TDS curves obtained by Novak et al. [84] for a high-strength AISI 4340 tempered martensitic steel, with each curve corresponding to a different controlled heating rate: 200, 100, and 50 °C/h. The conventional optimisation and ML analyses were conducted separately for each TDS spectrum. The material and data generation parameters were kept constant across all analyses. Conversely, the test parameters differed by one variable, the heating rate, which necessitated the use of different ML models for each case. As a result, three distinct multi-NN models were trained, each corresponding to one of the TDS spectra.

Test parameters were selected based on the values reported by the authors. The sample thickness was set to $L = 0.0063$ m, as specified, with the minimum and maximum temperatures set to $T_{\min} = 293.15$ K (20 °C) and $T_{\max} = 873.15$ K (600 °C). The resting time was not explicitly stated. Here, we assume this to be 45 min ($t_{\text{rest}} = 2700$ s), a typical resting time. As noted by Raina et al. [37], the resting time can significantly influence the desorption spectrum, particularly the initial flux values. Hence, this introduces a potential source of error between our predictions and the actual trapping parameters. Material parameters were taken from the properties characteristic of the bcc lattice, see Table 1, as the material in question is a tempered martensitic steel. This table also includes the molar mass, M_M , and the density ρ_M , which are required to convert the TDS hydrogen fluxes between the reported units of wppm, and the units of mol/m³ used throughout our work.

The data generation parameters were chosen by identifying a realistic range of trapping binding energies and densities that would produce fluxes matching the magnitudes of the observed TDS spectra. The range for absolute binding energies was set between 50 and 150 kJ/mol, with a minimum difference between binding energies of 10 kJ/mol. Trap densities were constrained to a range of 0.1–10 mol/m³ (6.022×10^{22} – 6.022×10^{24} sites/m³). The ML models were trained with 50,000 data points to predict a maximum of 4 traps. For the conventional optimisation analysis, the default settings in TDS Simulator were employed for the numerical simulation parameters (200 temperature evaluations and 100 discretisation elements) and for the global optimisation algorithm, as per the referenced study [43].

The results of the conventional optimisation analysis for all heating rates are presented in Fig. 9, showing both the simulated desorption

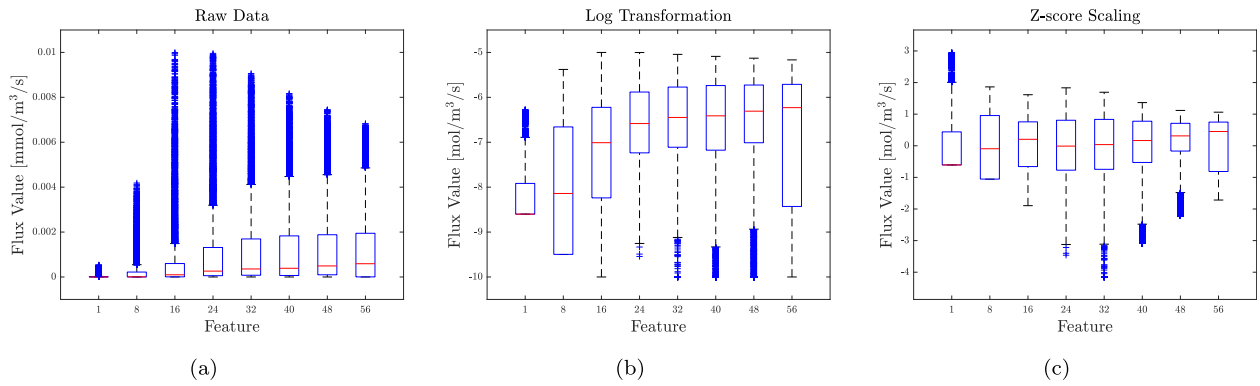


Fig. 8. Box-plots showing the distribution of eight selected features at each pre-processing stage: (a) raw data, (b) log-transformed data, and (c) log-transformed data with z-score scaling. Each feature represents the desorption flux value corresponding to a distinct temperature of the TDS spectrum. The selected features are evenly distributed across the temperature range, representing the overall feature set. The pre-processing steps progressively reduce skewness and standardise the data, aiming to approximate a normal distribution with zero mean and comparable variance across all features.

Table 1

Typical values of relevant material parameters for a bcc lattice.

Source: Data taken from [43].

Metal/alloy	E_L [kJ/mol]	D_0 [m ² /s]	M_M [g/mol]	ρ_M [g/cm ³]	N_L [sites/m ³]	C_L^0 [mol/m ³]
Bcc lattice	5690	7.23×10^{-8}	55.847	7.847	5.1×10^{29}	0.06

curves and the individual trap contributions. The optimisation algorithm is able to find TDS spectra that accurately follow the experimental data, successfully capturing the major features. Across all heating rates, the underlying trapping behaviour remained consistent, as reflected in the repeated identification of three dominant traps. These exhibited similar binding energies: Trap 1 ranged from -47 to -54 kJ/mol (blue peak), Trap 2 from -64 to -72 kJ/mol (orange peak), and Trap 3 from -94 to -98 kJ/mol (yellow peak). While slight variations in absolute trap densities were observed, their relative contributions to the dominant peak remained stable. A fourth, high-energy, low-density trap (purple peak) appeared only at the intermediate heating rate of $\phi = 100$ °C/h.

The results obtained using the ML approach are shown in Fig. 10. For all heating rates, the ML predictions closely replicate the main features of the experimental spectra, capturing both the prominent low-temperature peaks and the smaller, higher-temperature peaks. Some minor quantitative discrepancies are noted at the lowest heating rate ($\phi = 50$ °C/h), particularly in the prominent peak height. The individual trap contributions identified by the ML model are shown in Fig. 11, again indicating consistent trapping behaviour across all heating rates. Specifically, the peak temperature corresponding to each trap type is almost identical across all spectra. Additionally, the order of trap type densities is the same (Trap 1 > Trap 2 > Trap 3 > Trap 4). The inferred binding energies are similar to those obtained from the conventional optimisation approach: Trap 1 ranged from -48 to -53 kJ/mol, Trap 2 from -61 to -75 kJ/mol, and Trap 3 from -90 to -96 kJ/mol. An additional trap (Trap 4) with binding energy ranging from -128 to -145 kJ/mol was identified for all heating rates.

The trap type corresponding to each identified peak can be determined by comparing the values of ΔH obtained in this study with similar ranges of values reported for various tempered martensitic steels. Several trap types can be attributed to peak 2, in particular those related to incoherent interfaces, such as prior-austenite grain boundaries [84,85]. The relatively high $|\Delta H|$ reported for peak 3 can instead be associated with only a few trap states, specifically incoherent carbides and carbon matrix interfaces [85]. Determining the trap type associated with peak 1 is less straightforward. Employing Kissinger's approach, Novak et al. [84] reported peak 1 to be associated with the elastic strain field of dislocations (or other martensitic interfaces), having $\Delta H = -18$ kJ/mol. In this study, Trap 1 was found to have

a value of ΔH ranging from -47 to -54 kJ/mol. Several studies have reported dislocations in tempered martensitic steels to have a $\Delta H = -25$ to -35 kJ/mol [80,81]. Given the underestimation in (absolute) binding energies associated with Kissinger's approach, it is reasonable to attribute Trap 1 to the presence of dislocations. Finally, peak 4 is most likely a consequence of experimental artefact. The trapping contribution is very small, and no trap sites are reported in literature having such large values of $|\Delta H|$.

A direct comparison of the trapping parameters—number of traps, binding energies, and densities—obtained through both conventional optimisation and ML approaches is presented in Fig. 12. The comparison highlights the quantitative differences between the two methods, particularly in terms of trap densities. For each heating rate, the inferred densities of each trap type differ slightly between the approaches. A prominent example is the trap densities of Trap 2 and Trap 3 for $\phi = 100$ °C/h. Conventional optimisation predicts densities of $N_T^{(2)} = 1.0 \times 10^{24}$ sites/m³ and $N_T^{(3)} = 8.6 \times 10^{23}$ sites/m³, while the ML approach predicts densities of $N_T^{(2)} = 1.5 \times 10^{24}$ sites/m³ and $N_T^{(3)} = 9.1 \times 10^{23}$ sites/m³. Differences are also evident for Trap 4, in both trap density and binding energy. Conventional optimisation predicts a density of $N_T^{(4)} = 1.0 \times 10^{24}$ sites/m³ and a binding energy of $\Delta H^{(4)} = -150.0$ kJ/mol, while the ML approach predicts a density of $N_T^{(4)} = 7.4 \times 10^{23}$ sites/m³ and a binding energy of $\Delta H^{(4)} = -128.9$ kJ/mol. The larger discrepancies for Trap 4, especially in binding energy, likely arise from the fact that this peak was not fully captured in the spectrum, which complicates the analysis and enhances the ill-posed nature of the problem.

Fig. 12 illustrates that while both the ML and conventional optimisation approaches are able to reproduce the spectra for different heating rates, the results for one heating rate cannot be extrapolated to other heating rates. As the same material was used for all tests, identical trapping parameters are expected across varying heating rates; however, this is not observed. For instance, the ML predictions show that Trap 3 for $\phi = 50$ °C has a density of $\Delta H^{(3)} = 4.6 \times 10^{23}$ sites/m³, significantly lower than that of the other two heating rates: $\Delta H^{(3)} = 8.1 \times 10^{23}$ sites/m³ at $\phi = 200$ °C and $\Delta H^{(3)} = 9.1 \times 10^{23}$ sites/m³ at $\phi = 100$ °C. Additionally, there is a noticeable difference in the binding energy of Trap 2, with a disparity of over 10 kJ/mol between $\phi = 200$ °C and the other two heating rates. These quantitative differences are highlighted when the parameters identified for each

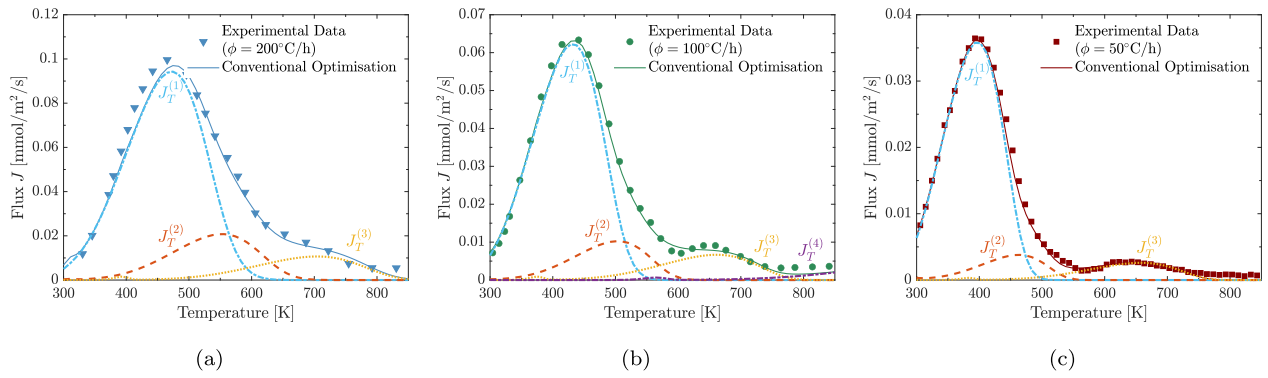


Fig. 9. Using conventional optimisation (TDS Simulator [43]) to gain insight into the trapping characteristics of a high-strength tempered martensitic steel. The experimental [84] and simulated desorption curves, with the latter being based on the trapping parameters fitted by TDS Simulator's optimisation algorithm, are presented for different temperature ramps: (a) $\phi = 200$ °C/h, (b) $\phi = 100$ °C/h, and (c) $\phi = 50$ °C/h. The contribution of each relevant trap type i , denoted $J_T^{(i)}$, as determined by TDS Simulator, is also depicted. The traps are reported in order of absolute binding energy $|\Delta H|$.

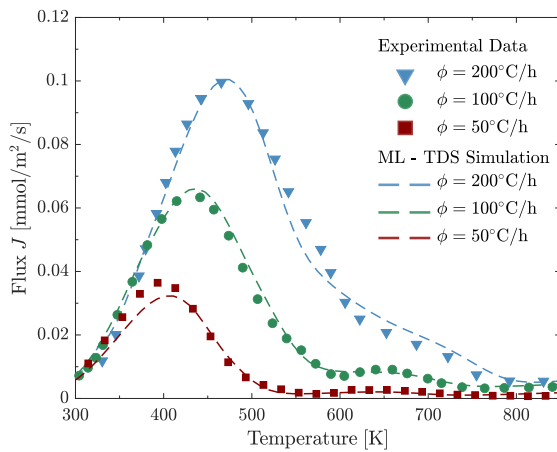


Fig. 10. Using our ML approach to gain insight into the trapping characteristics of a high-strength tempered martensitic steel. The experimental [84] and simulated desorption curves, with the latter being based on the trapping parameters fitted by the ML models, are presented for different temperature ramps: $\phi = 200$ °C/h, $\phi = 100$ °C/h, and $\phi = 50$ °C/h.

heating rate are used to generate the spectra of the other heating rates (Fig. 13). Mismatches in terms of both peak location and height can be observed between the simulated spectra and the experimental data. This mismatch has been observed in several studies, especially at higher heating rates [35,43,86]. It has been argued that these discrepancies are due to deviations of the experimental temperature ramp from the assumed linear ramp used in theoretical models. Such deviations may arise from laboratory setups that cannot ensure a perfectly linear or reproducible temperature ramp. Since key material parameters (such as D_L , $k^{(i)}$ and $p^{(i)}$) are governed by Arrhenius relationships, minor temperature differences can have a significant effect. There is also an inevitable sample-to-sample variability, and the deviation from the experimental data could well fall within the experimental scatter. Nevertheless, both sample-to-sample variability and temperature profile errors are becoming smaller in modern TDS systems.

4.2. Tempered martensitic Fe-C-Ti alloy

For the second example, the ML approach is employed to determine the trapping characteristics of a Fe-C-Ti alloy, containing 0.1 wt% C and a stoichiometric amount of Ti, which was investigated by Depover et al. [29]. Before TDS testing, the alloy was quenched to obtain a full martensitic structure and subsequently subjected to tempering at 600 °C

for 1 h, for the generation of TiC precipitates. The same protocol as in the previous test case for defining the parameters is followed. The thickness of the sample and heating rate were defined as $L = 0.001$ m and 600 °C/h ($\phi = 0.167$ K/s), respectively, as specified in the original study. In terms of the other test parameters, the resting time was taken as $t_{\text{rest}} = 3600$ s. Finally, the minimum and maximum temperatures were defined as $T_{\text{min}} = 293.15$ K and $T_{\text{max}} = 873.15$ K. Given that the material in question is a tempered martensitic steel, the relevant lattice properties were taken as the properties characteristic of the bcc lattice (Table 1).

The TDS spectra of tempered martensitic samples are often characterised by a low-energy high-density trap, which can be attributed to the sum of several defects with similar ΔH , such as dislocations and martensitic lath boundaries [48]. The data generation process was altered to account for these types of spectra. Simply expanding the allowable trap binding energy and density ranges is not a viable option. It was observed that model performance severely degrades when dealing with very large density ranges—particularly those exceeding two orders of magnitude. Additionally, due to the random nature of the trap characteristic generation process, there is a possibility that traps with low binding energies and low densities are generated. In such cases, there is a risk that the hydrogen from these traps desorbs during the rest period. As a result, these traps will not have a corresponding peak in the TDS spectrum, which can have an adverse impact on model training and performance.

To improve the quality of the training data—specifically, how closely it resembles the experimental data—without compromising the accuracy and efficiency of the model, the data generation process is modified by separating the trapping characteristic generation phase into two steps. In the first step, the characteristics of the low-energy, high-density trap, also referred to as the first trap, are randomly generated. In the second step, the characteristics of the remaining traps are defined. This separation ensures the correct energy and density ranges are assigned for the random generation of each trap. The data generation parameters for each step were chosen by selecting a realistic range of trapping binding energies and densities that would produce fluxes consistent with the magnitudes observed in the TDS spectra. For the first trap, the absolute binding energy range is set between 30 kJ/mol and 50 kJ/mol, with the density range between 40 and 100 mol/m³ ($2.409 \times 10^{25} - 6.022 \times 10^{25}$ sites/m³). For the other traps, the absolute binding energy range is set between 50 kJ/mol and 110 kJ/mol, with densities ranging from 0.1 mol/m³ to 10 mol/m³ ($6.022 \times 10^{22} - 6.022 \times 10^{24}$ sites/m³). The minimum difference between binding energies was set to 10 kJ/mol, and the ML models were trained for a maximum number of 4 traps. The ML models were first trained with 50,000 data points; subsequently, the analysis was repeated with 100,000 data points. Doubling the number of training

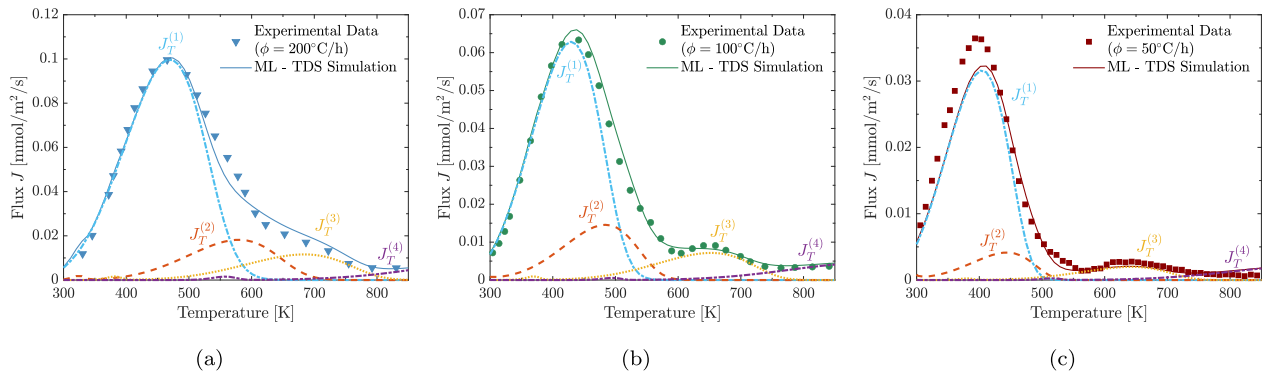


Fig. 11. Contribution of each relevant trap type i to the hydrogen desorption spectrum, denoted $J_T^{(i)}$, for different temperature ramps: (a) 200 °C/h, (b) 100 °C/h, and (c) 50 °C/h, as determined by the ML approach. The traps are reported in order of absolute binding energy $|\Delta H|$.

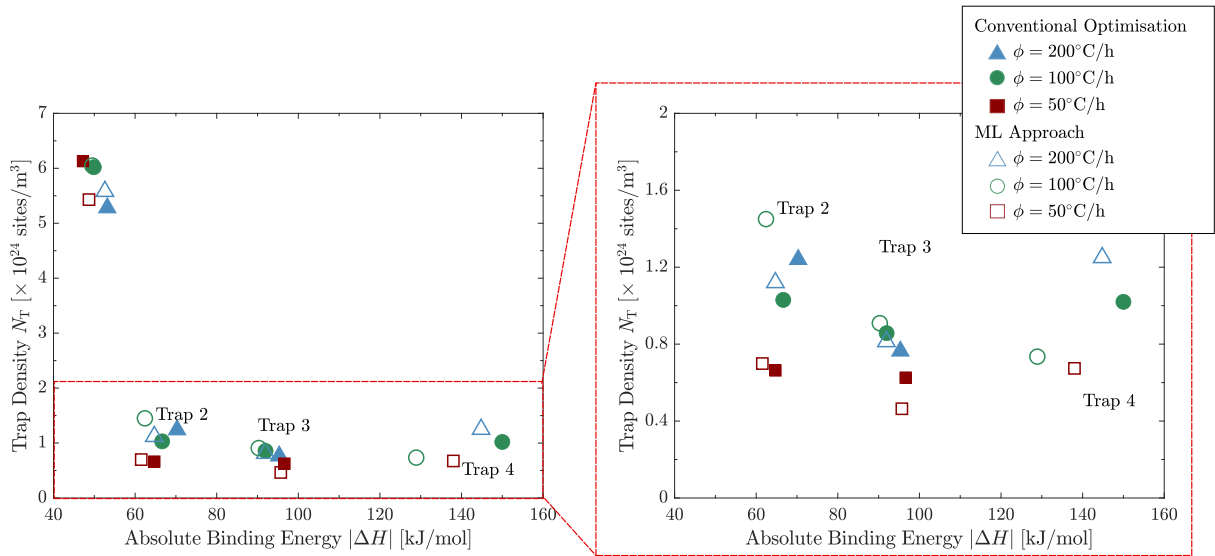


Fig. 12. Scatter plot comparing the absolute binding energies ($|\Delta H|$) and trap densities (N_T) obtained using conventional optimisation (TDS Simulator [43]) and ML approaches. The plot illustrates the agreement between the two approaches in predicting the trapping characteristics of a high-strength tempered martensitic steel from experimental TDS spectra for different temperature ramps: 200 °C/h, 100 °C/h, 50 °C/h. The traps are reported in order of absolute binding energy $|\Delta H|$.

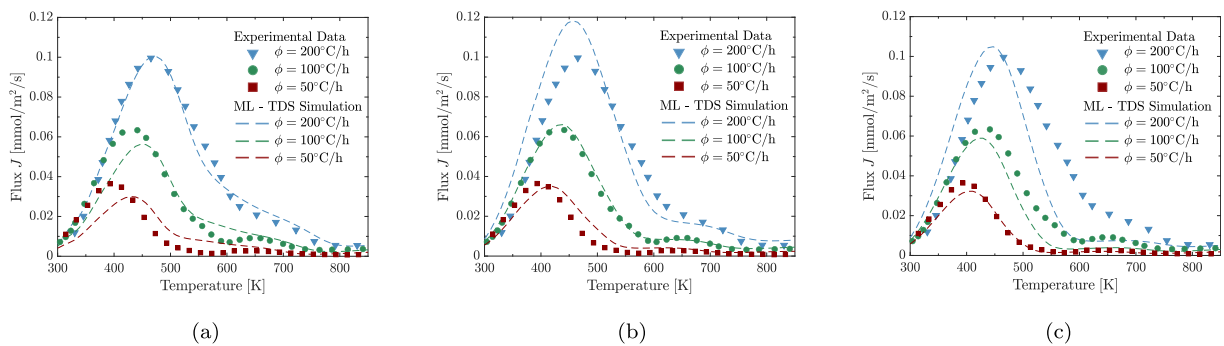


Fig. 13. Comparison of simulated and experimental TDS data of high-strength tempered martensitic steel [84] at various heating rates. Simulated desorption curves use trapping parameters predicted by the ML models for experimental spectra obtained with temperature ramps of: (a) 200 °C/h, (b) 100 °C/h, and (c) 50 °C/h.

data points had no significant effect, as discussed below. The same numerical simulation parameters and fitting procedure required for the conventional optimisation approach were adopted as in the previous test case.

The conventional optimisation and ML approach predictions are illustrated in Fig. 14, showing both the simulated desorption curves and individual trap contributions. Specifically, Fig. 14(a) presents the reconstructed spectrum based on trapping parameters fitted via the

conventional optimisation approach, while Fig. 14(b) and Fig. 14(c) show the spectra reconstructed from the trapping parameters predicted by ML models trained on 50,000 and 100,000 data points, respectively. The results obtained by each approach show similar qualitative trends but differ quantitatively, particularly in the number of traps identified. The trapping parameters inferred by the conventional optimisation approach reveal that the desorption curve can be deconvoluted into five peaks, each associated with a distinct trap type. Conversely, both

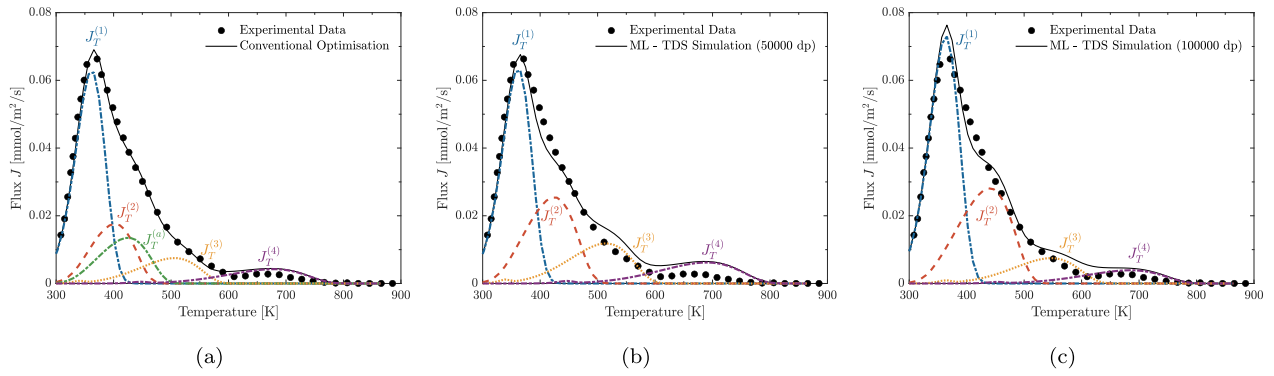


Fig. 14. Gaining insight into the trapping characteristics of a tempered martensitic Fe-C-Ti alloy. Comparison between experimental [29] and simulated desorption curves, with the latter being obtained using the trapping parameters as determined by (a) conventional optimisation (TDS Simulator [43]), (b) ML models trained with 50,000 data points and (c) ML models trained with 100,000 data points. The contributions of each relevant trap type i , denoted $J_T^{(i)}$, as determined by each respective approach, are also illustrated. The traps are reported in order of absolute binding energy $|\Delta H|$. The additional trap identified by the conventional optimisation (TDS Simulator) approach is referred to as $J_T^{(a)}$.

ML analyses report only four trap types. Each trap predicted by the ML models can be matched to a trap inferred by the conventional optimisation approach, considering similarities in peak temperature and height. These traps are reported in order of absolute binding energies $|\Delta H|$ (see Fig. 14). The additional trap identified by the conventional optimisation approach, shown in Fig. 14(a), is referred to as Trap a.

Reconstructing the TDS spectrum based on the fitted parameters obtained using the conventional optimisation approach produced an excellent match, capturing all major features of the desorption curve (see Fig. 14(a)). The most prominent peak is governed by a low-energy ($\Delta H^{(1)} = -36.9$ kJ/mol) high density ($N_T^{(1)} = 4.33 \times 10^{25}$ sites/m³) trap, which is attributed to a collection of defects with similar binding energies, typically associated with the martensitic microstructure (e.g., lath boundaries and dislocations) [48]. The smooth drop in the desorption rate following this peak is caused by three traps, linked to carbon vacancies at the carbide/matrix interface [48]. Two of these three traps share very similar characteristics: binding energies of $\Delta H^{(2)} = -56.2$ kJ/mol and $\Delta H^{(a)} = -61.1$ kJ/mol, with trap densities of $N_T^{(2)} = 1.41 \times 10^{24}$ sites/m³ and $N_T^{(a)} = 1.09 \times 10^{24}$ sites/m³, respectively. The third trap in this group has a stronger binding energy ($\Delta H^{(3)} = -76.3$ kJ/mol) and a lower trap density ($N_T^{(3)} = 7.0 \times 10^{23}$ sites/m³). The slight difference in ΔH between the former two traps and the latter one is the type of interface in which the carbon vacancies are found. Atomistic simulations were conducted by Di Stefano et al. [87] to understand the interaction of hydrogen with TiC in iron and provide a more in-depth understanding of the difference in trap sites. Binding energies of -44 kJ/mol and -87 kJ/mol were reported for the (001)- and (110)-interface, respectively. Thus, Trap 3 can be attributed to the (110)-interface. Conversely, Trap 2 and a are most likely connected to the (001)-interface as they have a lower absolute ΔH . Finally, the high-temperature peak observed around 700 K corresponds to a deep trap with a strong binding energy of $\Delta H^{(4)} = -107.4$ kJ/mol and a low trap density ($N_T^{(4)} = 5.10 \times 10^{23}$ sites/m³). This trap can be associated with carbon vacancies within the TiC precipitates [88].

The TDS curve reconstructed from the predictions of the ML model trained with 50,000 data points exhibits good agreement with the experimental data at the low-temperature peak (see Fig. 14(b)). However, notable discrepancies are observed at the high-temperature peak, where the model significantly overestimated the density. Additionally, mismatches are visible on the right-hand side of the low-temperature peak. The first trap, which dominates the prominent low-temperature peak, was identified by the ML model as having a binding energy of $\Delta H^{(1)} = -37.3$ kJ/mol and trap density of $N_T^{(1)} = 3.78 \times 10^{25}$ sites/m³, consistent with the conventional optimisation results. However, the traps responsible for the smooth drop in desorption differ from the conventional model. The ML model identified only two traps instead

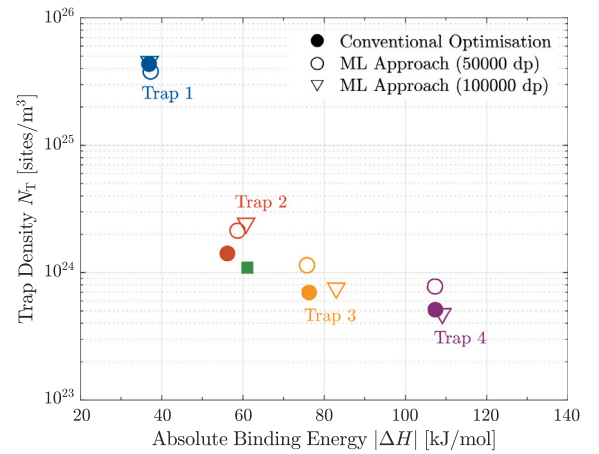


Fig. 15. Scatter plot comparing the absolute binding energies ($|\Delta H|$) and trap densities (N_T) obtained using conventional optimisation (TDS Simulator [43]) and ML approaches. The plot illustrates the agreement between the two approaches in predicting the trapping characteristics of a tempered martensitic Fe-C-Ti alloy from experimental data [29]. The traps are reported in order of absolute binding energy $|\Delta H|$. The additional trap identified by the conventional optimisation (TDS Simulator [43]) approach is depicted in green. The y-axis is shown on a logarithmic scale.

of three, with binding energies of $\Delta H^{(2)} = -58.7$ kJ/mol and $\Delta H^{(3)} = -75.8$ kJ/mol, and densities of $N_T^{(2)} = 2.13 \times 10^{24}$ sites/m³ and $N_T^{(3)} = 1.14 \times 10^{24}$ sites/m³, respectively. The final trap, corresponding to the high-temperature peak, showed similar parameters to those from the conventional approach, with $\Delta H^{(4)} = -107.3$ kJ/mol and $N_T^{(4)} = 7.77 \times 10^{23}$ sites/m³. To improve the ML model predictions, the analysis was repeated with 100,000 training data points (see Fig. 14(c)). Despite the increased volume of training data, no significant improvement in model performance is observed. Similar trapping parameters were found as for the 50,000 training data points case. While the ML model captured the more complex features of the TDS curve—particularly the regions near the low-temperature peak—it severely overestimated the density at the low-temperature peak. The limited improvement can be attributed to the data generation process, which is based on random distributions and may not adequately capture the underlying patterns required for effective learning. In ANN, increasing the quantity of training data does not guarantee enhanced model performance if the data is not sufficiently representative, as the model may struggle to extract meaningful features or generalise beyond the training data.

The agreement between the quantification techniques is assessed by comparing the inferred trapping parameters in Fig. 15. The traps

are labelled as defined in Fig. 14. Strong agreement between the approaches is observed for Traps 1 and 4, while the agreement is weaker for Traps 2 and 3. The ML model's inability to adequately fit the experimental data around the peaks corresponding to Traps 2 and 3 might be partly due to the model being trained with an incorrect maximum number of traps. The conventional optimisation approach showed that the experimental TDS curve can be accurately reproduced using a total of five traps, including an intermediate trap between Traps 2 and 3 with a binding energy differing by less than 5 kJ/mol from that of Trap 2 (see Fig. 14(a)). In contrast, the ML model was limited to a maximum of four traps and a minimum binding energy difference of 5 kJ/mol, preventing it from accurately deconvoluting this region into three separate traps. Although increasing the maximum number of traps in the ML model could potentially improve the experimental data fit, doing so is currently impractical due to the associated computational costs. The architecture of both NNs scales with the number of outputs, so increasing from four to five traps (i.e., 8 to 10 outputs for the regression model and 4 to 5 outputs for the classification model) significantly expands the number of trainable parameters. This not only increases training time and memory requirements but also demands a larger dataset to avoid over-fitting and ensure model generalisation. Given that the current model already showed limitations when trained on 100,000 data points for four traps, a substantially larger dataset would be required for five traps, making the approach computationally expensive.

4.3. Tempered martensitic Fe-0.05C-0.20Ti-2.0Ni alloy

The third test case involves the TDS spectrum of a tempered martensitic Fe-0.05C-0.20Ti-2.0Ni alloy, obtained by Wei and Tsuzaki [31]. The values reported by the authors were used to define the test parameters. The thickness of the sample and heating rate were taken as $L = 0.005$ m and 100 °C/h ($\phi = 0.0278$ K/s), respectively. The resting time, not specified by the authors, was estimated as $t_{\text{rest}} = 120$ s based on the initial drop in desorption rate observed in the spectrum. Finally, the minimum and maximum temperatures were defined as $T_{\text{min}} = 293.15$ K and $T_{\text{max}} = 1200$ K. Similar to the previous two test cases, material parameters were taken from the properties characteristic of the ferritic lattice, see Table 1, as the material under investigation is a tempered martensitic steel. Given that Wei and Tsuzaki [31] use a recombination poison (NH_4SCH) to enhance hydrogen uptake, an initial lattice hydrogen concentrations C_L^0 ten times greater than that reported for ferritic lattices ($C_L^0 = 0.6$ mol/m³) is employed in this study.

Similar to test case two, the alloy in question contains Ti carbides. However, comparing the spectrum of the Fe-0.05C-0.20Ti-2.0Ni alloy to that of the Fe-C-Ti alloy of the former test case, key differences can be observed. The most critical difference is the initial drop in desorption rate in the spectrum of the Ti carbide containing steel, which is absent in that of the Fe-C-Ti alloys. This spike is due to rapid desorption and originates from the presence of a high-density, low-energy trap. It is a direct consequence of the short resting time adopted by Wei and Tsuzaki [31]. To account for this low-energy, high-density trap, the data generation process is modified by separating the trapping characteristic generation phase into two steps, following the procedure described in the previous case study (Section 4.2). For the first trap, the range for absolute binding energies was set between 10 and 20 kJ/mol, while trap densities were constrained to a range of $1 \times 10^4 - 1 \times 10^5$ mol/m³ ($6.022 \times 10^{27} - 6.022 \times 10^{28}$ sites/m³). For the remaining traps, the range for absolute binding energies was set between 40 and 140 kJ/mol, with a minimum difference between binding energies of 10 kJ/mol. Trap densities were constrained to a range of $1-20$ mol/m³ ($6.022 \times 10^{23} - 1.2044 \times 10^{25}$ sites/m³). The more restricted density range of these traps was introduced to minimise any interference with model performance, as it was observed in the previous case studies that density ranges spanning more than two orders of magnitude cause a substantial deterioration in the model's predictive

capability. Relative to the previous case studies, a greater magnitude of Gaussian noise, with a standard deviation of 0.1, was necessary to improve the quality of the fit. The ML models were trained with 50,000 data points to predict a maximum of 4 traps. In regard to the conventional optimisation approach, the default numerical simulation and fitting parameters were used, as in the previous case studies.

The results of the conventional optimisation and ML analyses are given in Fig. 16. First, Fig. 16(a) shows the simulated desorption curve based on the conventional optimisation predictions alongside experimental data. As in the previous test cases, the conventional optimisation approach is able to produce an excellent fit, capturing all major features of the TDS curve. The analysis reveals that the spectrum can be deconvoluted into four peaks, each corresponding to a distinct trap. Similar results are obtained by the ML approach as shown in Fig. 16(b). The ML approach is able to capture the characteristics of the desorption spectra very well, from the initial drop in desorption rate to the smallest ones that appear at higher temperatures. A slight mismatch is observed between the experimental data and ML model predictions at the initial drop in desorption rate. As in the conventional optimisation approach, the response is captured by four traps. Good agreement is observed between the two approaches. Comparing the trap contributions in each spectrum (see Fig. 16), similar qualitative trends can be observed. Specifically, the peak temperature corresponding to each trap type is almost identical across both approaches. Additionally, the order of trap type densities is the same for all spectra (Trap 1 > Trap 2 > Trap 3 > Trap 4).

Subsequent analysis and comparison of the trapping parameters inferred by each approach provide greater insight into the trapping characteristics of the tempered martensitic Fe-0.05C-0.20Ti-2.0Ni alloy, as well as the agreement between the two quantification techniques (shown in Fig. 17). Very similar trap densities and binding energies are reported by the approaches, specifically for Traps 2 to 4. A larger discrepancy is observed in both trapping parameters of Trap 1. Both approaches attribute the initial spike in desorption to a shallow trap (Trap 1) with a significantly higher density, by four orders of magnitude, compared to the other traps. The conventional optimisation method assigns this trap a binding energy of $\Delta H^{(1)} = -15.0$ kJ/mol and a density of $N_T^{(1)} = 1.08 \times 10^{28}$ sites/m³, while the ML approach predicts a slightly lower binding energy of $\Delta H^{(1)} = -12.9$ kJ/mol and a higher density of $N_T^{(1)} = 1.30 \times 10^{28}$ sites/m³. The difference of 3 kJ/mol in binding energy between the two methods helps explain the mismatch between the ML-predicted and experimental curves observed in Fig. 16(b) at the initial desorption drop. The prominent low-temperature peak in the desorption data was found to result from the presence of two traps (Traps 2 and 3). Using the conventional optimisation approach, their binding energies and densities were determined as $\Delta H^{(2)} = -47.8$ kJ/mol and $\Delta H^{(3)} = -64.1$ kJ/mol, and $N_T^{(2)} = 7.50 \times 10^{24}$ sites/m³ and $N_T^{(3)} = 3.36 \times 10^{24}$ sites/m³, respectively. In comparison, the ML approach predicted $\Delta H^{(2)} = -48.3$ kJ/mol and $\Delta H^{(3)} = -62.7$ kJ/mol, and $N_T^{(2)} = 8.85 \times 10^{24}$ sites/m³ and $N_T^{(3)} = 2.78 \times 10^{24}$ sites/m³ for the same traps. Based on typical values reported in the literature, these traps can be attributed to grain boundaries, dislocations, and coherent TiC. Finally, the high-temperature peak located around 800–900 K is attributed to a deep trap (Trap 4) associated with incoherent TiC particles. Similar binding energies of $\Delta H^{(4)} = -122.2$ kJ/mol and $\Delta H^{(4)} = -120.5$ kJ/mol and trap densities of $N_T^{(4)} = 1.04 \times 10^{24}$ sites/m³ and $N_T^{(4)} = 1.19 \times 10^{24}$ sites/m³ were reported by the conventional optimisation and ML approach, respectively.

4.4. Comparison of the trapping characteristics of tempered martensitic steels

A comparison of the trapping characteristics predicted by the newly developed ML approach for each tempered martensitic steel is presented in Table 2. Due to the microstructural similarities among the three alloys, several common trapping features were observed. Notably,

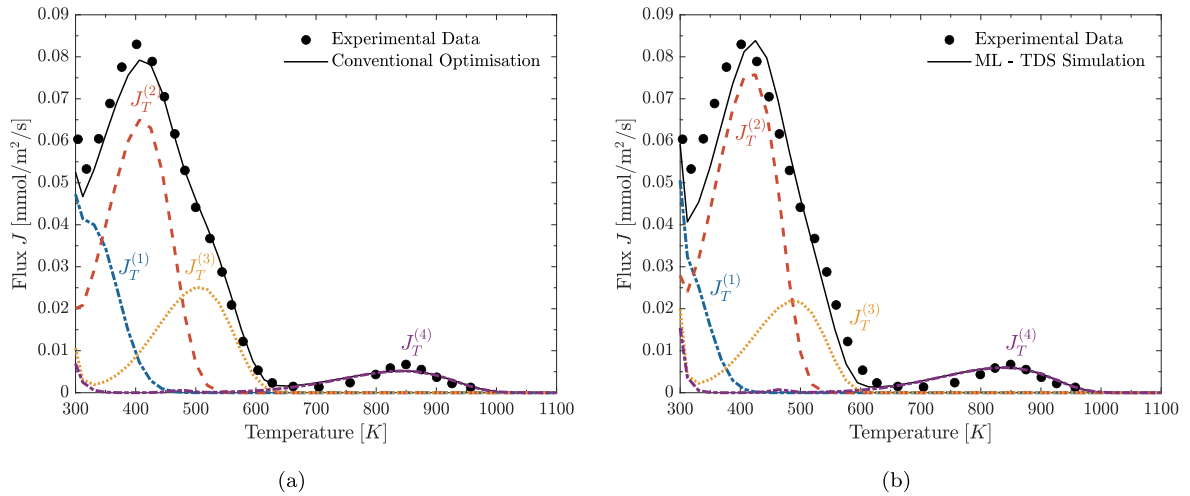


Fig. 16. Gaining insight into the trapping characteristics of a tempered martensitic Fe-0.05C-0.20Ti-2.0Ni alloy. Comparison between experimental [31] and simulated desorption curves, with the latter being obtained using the trapping parameters as determined by (a) conventional optimisation (TDS Simulator [43]), and (b) the present ML approach. The contributions of each relevant trap type i , denoted $J_T^{(i)}$, as determined by each respective approach, are also illustrated. The traps are reported in order of absolute binding energy $|\Delta H|$.

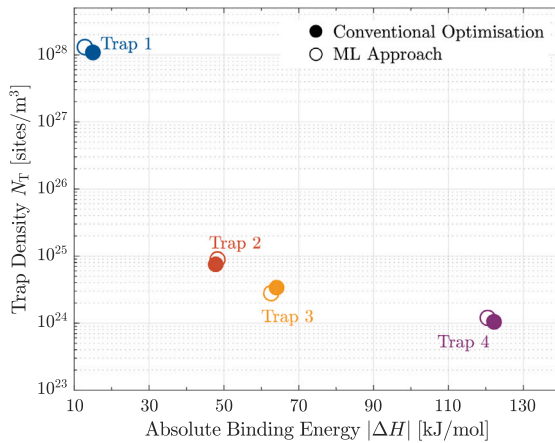


Fig. 17. Scatter plot comparing the absolute binding energies ($|\Delta H|$) and trap densities (N_T) obtained using conventional optimisation (TDS Simulator [43]) and ML approaches. The plot illustrates the agreement between the two approaches in predicting the trapping characteristics of a tempered martensitic Fe-0.05C-0.20Ti-2.0Ni alloy from experimental data [31]. The traps are reported in order of absolute binding energy $|\Delta H|$. The y-axis is shown on a logarithmic scale.

all steels exhibited a low-energy, high-density trap—identified as Trap 1 for the high-strength AISI 4340 and Fe-C-Ti alloys (Test Cases 1 and 2), and as Traps 1 and 2 for the Fe-0.05C-0.20Ti-2.0Ni alloy (Test Case 3). These traps are likely associated with typical martensitic features such as dislocations and lath boundaries [6,31,48]. Additionally, all alloys showed a trap in the 60–75 kJ/mol binding energy range, most likely corresponding to coherent carbides or carbide-matrix interfaces [6,48,87]. A key distinction was observed in Test Case 3, which exhibited a significantly stronger trapping site with a binding energy of 120.5 kJ/mol [31]. This high-energy trap is attributed to the presence of incoherent TiC particles, which are not found in the other two alloys.

4.5. Limitations

While the ML models provide good fits to the experimental datasets, the conventional optimisation approach results in more accurate predictions across all test cases. This is primarily due to the ability of the PSO algorithm to refine its predictions with increasing runtime. In

contrast, once trained, the ML models provide a single prediction for a given input. Improving the predictions requires retraining the model with an increased volume of training data. Even then, retraining does not always guarantee improved performance. Moreover, the dataset and training used in the ML approach are specific to the TDS test and material parameters (e.g., lattice diffusivity, heating rate, sample thickness). As a result, each ML model is not generalisable to experimental datasets that differ significantly from the conditions it was trained on. However, TDS parameters (e.g., sample size) typically remain consistent across experiments, and the relevant material parameters (e.g., lattice diffusivity) are common to a wide range of materials (being lattice properties). As such, the training of the present TDS-ML approach on representative test parameters and material classes (fcc, bcc) would enable efficient predictions across alloys within the same class — e.g., quantifying the role of micro-structural and compositional changes on trapping characteristics. Additionally, since training and data generation can be completed before the experiments, the model allows for rapid, near-instantaneous processing of experimental data. For certain applications, the ML approach offers clear advantages over the conventional optimisation approach, which is time-consuming, as optimisation must be performed separately for each experiment, and may not reach the optimal solution if the optimisation algorithm encounters a local minimum.

However, there are other limitations associated with the ML approach that must also be taken into consideration. One additional challenge encountered was the sensitivity of the ML model to features poorly captured by the TDS spectrum. If the sample rest time (the time the sample is kept at room temperature before the start of the temperature ramp) is too short, part of the spectrum captures the diffusion of lattice hydrogen out of the sample, creating a peak at the start of the spectrum. As this peak is not uniquely defined (i.e., many possible combinations of trapping energy/density can result in a similar peak), the ML approach has issues properly learning how to identify the trapping energies and densities.

One final limitation of the ML approach is related to the range of trapping densities used within the model. Despite the scaling employed in the ML model, the scheme was only able to predict trapping densities across two orders of magnitude. This is also due to the limitations of pre-trained artificial neural networks. If extremely high and low densities are combined within a single model, the low-density peaks are overshadowed by the high-density peaks. As a result, the model is able to learn to identify the high-density trapping parameters, but is unable to identify the low-density traps.

Table 2

Comparison of the hydrogen trapping characteristics, i.e., the absolute binding energies and trap densities, extracted using the novel machine learning approach for three tempered martensitic steels with varying compositions. Test case 1 corresponds to high-strength AISI 4340 steel [84], Test case 2 to a Fe-C-Ti alloy [29], and Test case 3 to a Fe-0.05C-0.20Ti-2.0Ni alloy [31].

		Trap 1	Trap 2	Trap 3	Trap 4
Test case 1	$ \Delta H $ (kJ/mol)	48.7–52.6	61.5–74.7	90.3–95.7	128.9–144.8
	N_T (sites/m ³)	$(5.4–6.1) \times 10^{24}$	$(0.70–1.5) \times 10^{24}$	$(4.6–9.1) \times 10^{23}$	$(0.67–1.3) \times 10^{24}$
Test case 2	$ \Delta H $ (kJ/mol)	37.0–37.3	58.7–60.8	75.8–83.0	107.3–109.1
	N_T (sites/m ³)	$(3.8–4.5) \times 10^{25}$	$(2.1–2.4) \times 10^{24}$	$(0.75–1.1) \times 10^{24}$	$(4.8–7.8) \times 10^{23}$
Test case 3	$ \Delta H $ (kJ/mol)	12.9	48.3	62.7	120.5
	N_T (sites/m ³)	1.3×10^{28}	8.9×10^{24}	2.8×10^{24}	1.2×10^{24}

Finally, it is essential to acknowledge the limitations inherent in the constitutive model used to generate the training data. The model is based on the McNabb-Foster and Oriani formulations, both of which assume isolated, sparsely distributed traps and therefore neglect any potential interactions between traps. While this assumption is generally valid for BCC materials due to their high diffusivity [44,48,86], it becomes less appropriate for materials with lower diffusivity, such as FCC alloys, where trapping behaviour is influenced by the distribution, morphology and interconnectivity of the traps [89]. In such cases, these interactions cannot be disregarded. Extending the present approach to these materials will require incorporating more complex trap interactions in the numerical model as well as accounting for microstructural effects.

5. Conclusions

We have presented a neural network-based machine-learning model able to identify the trapping characteristics from thermal desorption experimental data. The model has been validated against the existing literature and its potential has been assessed through multiple case studies, extensively discussing its limitations and capabilities. The main advantages of this approach, relative to state-of-the-art TDS optimisation fitting approaches, are:

- The model is trained on purely numerical simulations, allowing it to be generated without needing any experimental inputs. This allows the models to be trained for a wide range of circumstances, providing an easy and quick way to process TDS curves to extract the trapping characteristics.
- The multi-ANN approach allows the number of unique traps to be first determined, and then automatically predicts the appropriate energies and densities for these trapping sites.
- In contrast to conventional optimisation schemes, the machine-learning-based model does not have any issues with convergence related to local minima, and is able to re-use the generated simulation data between studies, making it a computationally cheaper method to quantify a series of TDS curves.

Among others, the results obtained show that,

- The model can efficiently find trapping characteristics (number of trap types, along with their densities and binding energies) that closely match experimental TDS spectra and that are in good agreement with the fitting resulting from conventional optimisation approaches
- Addition of Gaussian noise to the training data is essential for accurately fitting experimental data, as synthetic data is noise-free, while real-world data is inherently noisy.
- Despite optimised input scaling techniques being employed in the model, the limitations of pre-trained neural networks and the ill-posed nature of the TDS analysis restrict the framework to predicting trap densities over a range of two orders of magnitude.

Future work will be aimed at overcoming the limitations of the model, discussed in Section 4.5, so as to further enhance its predictive capabilities. A primary goal will be to improve the scalability of the approach, enabling the development of a model applicable to an entire material class (e.g., bcc alloys) and typical TDS test parameters.

CRedit authorship contribution statement

Nicoletta Marrani: Writing – review & editing, Writing – original draft, Software, Visualization, Validation, Methodology, Investigation, Formal analysis, Data curation, Conceptualization. **Tim Hageman:** Writing – review & editing, Writing – original draft, Methodology, Supervision, Software, Resources, Conceptualization. **Emilio Martínez-Pañeda:** Writing – review & editing, Supervision, Resources, Project administration, Investigation, Funding acquisition, Conceptualization.

Declaration of competing interest

The authors declare that they have no known competing financial interests or personal relationships that could have appeared to influence the work reported in this paper.

Acknowledgements

N. Marrani and E. Martínez-Pañeda acknowledge support through the UKRI Horizon Europe Guarantee programme (ERC Starting Grant *ResistHfracture*, EP/Y037219/1). T. Hageman acknowledges support via the Royal Commission for the Exhibition of 1851 fellowship scheme and the John Fell Oxford University Press Research Fund. E. Martínez-Pañeda also acknowledges support from UKRI's Future Leaders Fellowship programme [grant MR/V024124/1]. The authors also acknowledge computational resources and support provided by the University of Oxford Advanced Research Computing Service (<http://dx.doi.org/10.5281/zenodo.22558>).

Data availability

The finite element simulation code and machine learning approaches employed are available at https://github.com/nicolettamarrani/TDS_ML_Approach.git and <https://mechmat.web.ox.ac.uk/codes>. Example inputs and files for post-processing, allowing the results from Fig 11 to be reproduced, are also included.

References

- [1] Moriarty P, Honnery D. Prospects for hydrogen as a transport fuel. *Int J Hydrog Energy* 2019;44(31):16029–37.
- [2] Genovese M, Schlüter A, Scionti E, Piraino F, Corigliano O, Fragiaco P. Power-to-hydrogen and hydrogen-to-X energy systems for the industry of the future in Europe. *Int J Hydrog Energy* 2023;48(44):16545–68.
- [3] Liu W, Zuo H, Wang J, Xue Q, Ren B, Yang F. The production and application of hydrogen in steel industry. *Int J Hydrog Energy* 2021;46(17):10548–69.
- [4] Pleshivtseva Y, Derevyanov M, Pimenov A, Rapoport A. Comprehensive review of low carbon hydrogen projects towards the decarbonization pathway. *Int J Hydrog Energy* 2023;48(10):3703–24.

- [5] Guo L, Su J, Wang Z, Shi J, Guan X, Cao W, Ou Z. Hydrogen safety: An obstacle that must be overcome on the road towards future hydrogen economy. *Int J Hydrog Energy* 2024;51:1055–78.
- [6] Chen Y-S, Huang C, Liu P-Y, Yen H-W, Niu R, Burr P, Moore KL, Martínez-Pañeda E, Atrens A, Cairney JM. Hydrogen trapping and embrittlement in metals – A review. *Int J Hydrog Energy* 2025;136:789–821.
- [7] Mandal TK, Parker J, Gagliano M, Martínez-Pañeda E. Computational predictions of weld structural integrity in hydrogen transport pipelines. *Int J Hydrog Energy* 2024.
- [8] Wijnen J, Parker J, Gagliano M, Martínez-Pañeda E. A computational framework to predict weld integrity and microstructural heterogeneity: Application to hydrogen transmission. *Mater Des* 2025;249:113533.
- [9] Martínez-Pañeda E. Progress and opportunities in modelling environmentally assisted cracking. *RILEM Tech Lett* 2021;6:70–7.
- [10] Hageman T, Martínez-Pañeda E. An electro-chemo-mechanical framework for predicting hydrogen uptake in metals due to aqueous electrolytes. *Corros Sci* 2022;208:110681.
- [11] Hageman T, Martínez-Pañeda E. A phase field-based framework for electro-chemo-mechanical fracture: Crack-contained electrolytes, chemical reactions and stabilisation. *Comput Methods Appl Mech Engrg* 2023;415:116235.
- [12] Schwarzer M, Hertl N, Nitz F, Borodin D, Fingerhut J, Kitsopoulos TN, Wodtke AM. Adsorption and Absorption Energies of Hydrogen with Palladium. *J Phys Chem C* 2022;2022:14500–8.
- [13] Cupertino-Malheiros L, Duportal M, Hageman T, Zafra A, Martínez-Pañeda E. Hydrogen uptake kinetics of cathodic polarized metals in aqueous electrolytes. *Corros Sci* 2024;231:111959.
- [14] Ferrin P, Kandoi S, Nilekar AU, Mavrikakis M. Hydrogen adsorption, absorption and diffusion on and in transition metal surfaces: A DFT study. *Surf Sci* 2012;606(7–8):679–89.
- [15] Zafra A, Harris Z, Korec E, Martínez-Pañeda E. On the relative efficacy of electropermeation and isothermal desorption approaches for measuring hydrogen diffusivity. *Int J Hydrog Energy* 2023;48(3):1218–33.
- [16] Lu X, Depover T, Johnsen R. Evaluation of hydrogen diffusion and trapping in nickel Alloy 625 by thermal desorption spectroscopy. *Int J Hydrog Energy* 2022;47(74):31673–83.
- [17] Cupertino-Malheiros L, Oudriss A, Thébault F, Piette M, Feaugas X. Hydrogen diffusion and trapping in low-alloy tempered martensitic steels. *Met Mater Trans A* 2023;54(4):1159–73.
- [18] Santos Maldonado C-T, Zafra A, Martínez Pañeda E, Sandmann P, Morana R, Pham M-S. Influence of dislocation cells on hydrogen embrittlement in wrought and additively manufactured Inconel 718. *Commun Mater* 2024;5(1):223.
- [19] Turnbull A. Perspectives on hydrogen uptake, diffusion and trapping. *Int J Hydrog Energy* 2015;40(47):16961–70.
- [20] Verbeken K. Analysing hydrogen in metals: bulk thermal desorption spectroscopy (TDS) methods. In: *Gaseous hydrogen embrittlement of materials in energy technologies*. Elsevier; 2012. p. 27–55.
- [21] Nagumo M, Takai K. The predominant role of strain-induced vacancies in hydrogen embrittlement of steels: Overview. *Acta Mater* 2019;165:722–33.
- [22] Depover T, Verbeken K. Thermal desorption spectroscopy study of the hydrogen trapping ability of w based precipitates in a Q & T matrix. *Int J Hydrog Energy* 2018;43(11):5760–9.
- [23] L JCG, Li W, Wang H, Zuo S, Jin X. Hydrogen trapping and desorption in TiVGrAl alloy fabricated by conventional and additive manufacturing. *Int J Hydrog Energy* 2025;139:1–10.
- [24] Shang J, Guo J, Hua Z, Xing B, Cui T, Wei H. Effects of plastic deformation on hydrogen trapping and hydrogen distribution in X80 pipeline steel. *Int J Hydrog Energy* 2025;136:1306–16.
- [25] Choo WY, Lee JY. Thermal analysis of trapped hydrogen in pure iron. *Met Trans A* 1982;13(1):135–40.
- [26] Van Veen A, Filius H, De Vries J, Bijkerk K, Rozing G, Segers D. Hydrogen exchange with voids in tungsten observed with TDS and PA. *J Nucl Mater* 1988;155–157:1113–7.
- [27] Lee S-M, Lee J-Y. Hydrogen trapping by voids in nickel. *Scr Metall* 1987;21(12):1655–8.
- [28] Yaktiti A, Dreano A, Carton J, Christien F. Hydrogen diffusion and trapping in a steel containing porosities. *Corros Sci* 2022;199:110208.
- [29] Depover T, Verbeken K. The effect of TiC on the hydrogen induced ductility loss and trapping behavior of Fe-C-Ti alloys. *Corros Sci* 2016;112:308–26.
- [30] Wei FG, Tsuzaki K. Quantitative analysis on hydrogen trapping of TiC particles in steel. *Met Mater Trans A* 2006;37(2):331–53.
- [31] Wei F-G, Hara T, Tsuchida T, Tsuzaki K. Hydrogen Trapping in Quenched and Tempered 0.42C-0.30Ti Steel Containing Bimodally Dispersed TiC Particles. *ISIJ Int* 2003;43(4):539–47.
- [32] Silverstein R, Eliezer D, Tal-Guttmacher E. Hydrogen trapping in alloys studied by thermal desorption spectrometry. *J Alloys Compd* 2018;747:511–22.
- [33] Kim S-G, Kim J-Y, Hwang B. Effect of tempering Temperature on Hydrogen Embrittlement of SCM440 Tempered Martensitic Steel. *Materials* 2023;16(16):5709.
- [34] Silverstein R, Eliezer D. Mechanisms of hydrogen trapping in austenitic, duplex, and super martensitic stainless steels. *J Alloys Compd* 2017;720:451–9.
- [35] Hurley C, Martin F, Marchetti L, Chêne J, Blanc C, Andrieu E. Numerical modeling of thermal desorption mass spectroscopy (TDS) for the study of hydrogen diffusion and trapping interactions in metals. *Int J Hydrog Energy* 2015;40(8):3402–14.
- [36] Kissinger HE. Variation of peak temperature with heating rate in differential thermal analysis. *J Res Natl Bur Stand* 1956;57(4):217.
- [37] Raina A, Deshpande V, Fleck N. Analysis of thermal desorption of hydrogen in metallic alloys. *Acta Mater* 2018;144:777–85.
- [38] McNabb A, Foster PK. A New Analysis of the Diffusion of Hydrogen in Iron and Ferritic Steels. *AIME* 1963;227:618–27.
- [39] Oriani R. The diffusion and trapping of hydrogen in steel. *Acta Metall* 1970;18(1):147–57.
- [40] Bombac D, Katzarov IH, Pashov DL, Paxton AT. Theoretical evaluation of the role of crystal defects on local equilibrium and effective diffusivity of hydrogen in iron. *Mater Sci Technol* 2017;33(13):1505–14.
- [41] Drexler A, Vandewalle L, Depover T, Verbeken K, Domitier J. Critical verification of the Kissinger theory to evaluate thermal desorption spectra. *Int J Hydrog Energy* 2021;46(79):39590–606.
- [42] Legrand E, Oudriss A, Savall C, Bouhattat J, Feaugas X. Towards a better understanding of hydrogen measurements obtained by thermal desorption spectroscopy using FEM modeling. *Int J Hydrog Energy* 2015;40(6):2871–81.
- [43] García-Macías E, Harris ZD, Martínez-Pañeda E. TDS Simulator: A MATLAB App to model temperature-programmed hydrogen desorption. *Int J Hydrog Energy* 2024;49:510–24.
- [44] Song EJ, Suh D-W, Bhadeshia H. Theory for hydrogen desorption in ferritic steel. *Comput Mater Sci* 2013;79:36–44.
- [45] Turnbull A, Hutchings R, Ferriss D. Modelling of thermal desorption of hydrogen from metals. *Mater Sci Eng: A* 1997;238(2):317–28.
- [46] Kirchheim R. Bulk Diffusion-Controlled Thermal Desorption Spectroscopy with Examples for Hydrogen in Iron. *Met Mater Trans A* 2016;47(2):672–96.
- [47] Delaporte-Mathurin R, Hodille EA, Mougenot J, Charles Y, Grisolia C. Parametric optimisation based on TDS experiments for rapid and efficient identification of hydrogen transport materials properties. *Nucl Mater Energy* 2021;27:100984.
- [48] Drexler A, Depover T, Verbeken K, Ecker W. Model-based interpretation of thermal desorption spectra of Fe-C-Ti alloys. *J Alloys Compd* 2019;789:647–57.
- [49] Carleo G, Cirac I, Cranmer K, Daudet L, Schuld M, Tishby N, Vogt-Maranto L, Zdeborová L. Machine learning and the physical sciences. *Rev Modern Phys* 2019;91(4):045002.
- [50] Sharifani K, Amini M. Machine Learning and Deep Learning: A Review of Methods and Applications. *World Inf Technol Engr J* 2023;10(07).
- [51] Karniadakis GE, Kevrekidis IG, Lu L, Perdikaris P, Wang S, Yang L. Physics-informed machine learning. *Nat Rev Phys* 2021;3(6):422–40.
- [52] García-Merino J, Calvo-Jurado C, Martínez-Pañeda E, García-Macías E. Multielement polynomial chaos Kriging-based metamodeling for Bayesian inference of non-smooth systems. *Appl Math Model* 2023;116:510–31.
- [53] Chauhan NK, Singh K. A Review on Conventional Machine Learning vs Deep Learning. In: *2018 international conference on computing, power and communication technologies (GUCON)*. Greater Noida, Uttar Pradesh, India: IEEE; 2018, p. 347–52.
- [54] Bhadeshia HKDH. Networks in Materials Science. *ISIJ Int* 1999;39(10):966–79.
- [55] Bock FE, Aydin RC, Cyron CJ, Huber N, Kalidindi SR, Klusemann B. Review of the Application of Machine Learning and Data Mining Approaches in Continuum Materials Mechanics. *Front Mater* 2019;vol. 6.
- [56] Jin H, Zhang E, Espinosa HD. Advances and Applications of Machine Learning in Experimental Solid Mechanics: A Review. *Appl Mech Rev* 2023;75(061001).
- [57] Thankachan T, Prakash KS, David Pleass C, Rammasamy D, Prabhakaran B, Jothi S. Artificial neural network to predict the degraded mechanical properties of metallic materials due to the presence of hydrogen. *Int J Hydrog Energy* 2017;42(47):28612–21.
- [58] Malitckii E, Fangnon E, Vilaça P. Evaluation of steels Susceptibility to Hydrogen Embrittlement: A Thermal Desorption Spectroscopy-Based Approach Coupled with Artificial Neural Network. *Materials* 2020;13(23):5500.
- [59] Malitckii E, Fangnon E, Vilaça P. Study of correlation between the steels susceptibility to hydrogen embrittlement and hydrogen thermal desorption spectroscopy using artificial neural network. *Neural Comput Appl* 2020;32(18):14995–5006.
- [60] Fangnon E, Malitckii E, Latypova R, Vilaça P. Prediction of hydrogen concentration responsible for hydrogen-induced mechanical failure in martensitic high-strength steels. *Int J Hydrog Energy* 2023;48(14):5718–30.
- [61] Oriani R. The physical and metallurgical aspects of hydrogen in metals. *Fusion Technol* 1994;26(4):235–66.
- [62] Kulagin V, Delaporte-Mathurin R, Hodille EA, Zibrov M. Kinetic surface model in festim: Verification and validation. *Int J Hydrog Energy* 2024;110:90–100.
- [63] Martínez-Pañeda E, Díaz A, Wright L, Turnbull A. Generalised boundary conditions for hydrogen transport at crack tips. *Corros Sci* 2020;173:108698.
- [64] Hageman T, Martínez-Pañeda E. Stabilising Effects of Lumped Integration Schemes for the Simulation of Metal-Electrolyte Reactions. *J Electrochem Soc* 2023;170(2):021511.
- [65] Dadfarnia M, Martin ML, Nagao A, Sofronis P, Robertson IM. Modeling hydrogen transport by dislocations. *J Mech Phys Solids* 2015;78:511–25.

- [66] Díaz A, Alegre JM, Cuesta II, Martínez-Pañeda E. A consol framework for predicting hydrogen embrittlement, part i: Coupled hydrogen transport. *Eng Fract Mech* 2025;319:111007.
- [67] Hoch BO, Metsue A, Bouhattate J, Feaugas X. Effects of grain-boundary networks on the macroscopic diffusivity of hydrogen in polycrystalline materials. *Comput Mater Sci* 2015;97:276–84.
- [68] Toribio J, Kharin V. A generalised model of hydrogen diffusion in metals with multiple trap types. *Phil Mag* 2015;95(31):3429–51.
- [69] Wang Y, Connétable D, Tanguy D. Influence of trap connectivity on h diffusion: Vacancy trapping. *Acta Mater* 2016;103:334–40.
- [70] Krom AHM, Bakker A. Hydrogen trapping models in steel. *Met Mater Trans B* 2000;31(6):1475–82.
- [71] Aggarwal C. An Introduction to Neural Networks. In: *Neural networks and deep learning. Neural networks and deep learning : a textbook*, Cham: Springer; 2023, p. 1–25.
- [72] Aggarwal C. Deep Learning: Principles and Training Algorithms. In: *Neural networks and deep learning: A Textbook*. Cham: Springer; 2023, p. 119–63.
- [73] Theodoridis S. Neural Networks and Deep Learning. In: *Machine learning*. Elsevier; 2020, p. 901–1038.
- [74] Abadi M, Agarwal A, Barham P, Brevdo E, Chen Z, Citro C, Corrado GS, Davis A, Dean J, Devin M, Ghemawat S, Goodfellow I, Harp A, Irving G, Isard M, Jia Y, Jozefowicz R, Kaiser L, Kudlur M, Levenberg J, Mane D, Monga R, Moore S, Murray D, Olah C, Schuster M, Shlens J, Steiner B, Sutskever I, Talwar K, Tucker P, Vanhoucke V, Vasudevan V, Viegas F, Vinyals O, Warden P, Wattenberg M, Wicke M, Yu Y, Zheng X. TensorFlow: Large-Scale Machine Learning on Heterogeneous Distributed Systems. 2015.
- [75] Chollet F, et al. Keras. 2015.
- [76] Santosh K, Das N, Ghosh S. Deep learning: a review. In: *Deep learning models for medical imaging*. Elsevier; 2022, p. 29–63.
- [77] Haque M. ANN back-propagation prediction model for fracture toughness in microalloy steel. *Int J Fatigue* 2002;24(9):1003–10.
- [78] Haque M. Prediction of corrosion-fatigue behavior of DP steel through artificial neural network. *Int J Fatigue* 2001;23(1):1–4.
- [79] Xu L, Xing J, Wei S, Zhang Y, Long R. Artificial neural network prediction of retained austenite content and impact toughness of high-vanadium high-speed steel (HVHSS). *Mater Sci Eng: A* 2006;433(1–2):251–6.
- [80] Li X, Ma X, Zhang J, Akiyama E, Wang Y, Song X. Review of Hydrogen Embrittlement in Metals: Hydrogen diffusion, Hydrogen characterization, Hydrogen Embrittlement Mechanism and Prevention. *Acta Met Sin (Engl Lett)* 2020;33(6):759–73.
- [81] Fernández-Sousa R, Betegón C, Martínez-Pañeda E. Analysis of the influence of microstructural traps on hydrogen assisted fatigue. *Acta Mater* 2020;199:253–63.
- [82] Yen S, Huang I. Critical hydrogen concentration for hydrogen-induced blistering on AISI 430 stainless steel. *Mater Chem Phys* 2003;vol. 80(3):662–6.
- [83] Yeo I-K, Johnson RA. A new family of power transformations to improve normality or symmetry. *Biometrika* 2000;vol. 87(4):954–9.
- [84] Novak P, Yuan R, Somerday B, Sofronis P, Ritchie R. A statistical, physical-based, micro-mechanical model of hydrogen-induced intergranular fracture in steel. *J Mech Phys Solids* 2010;58(2):206–26.
- [85] Li D, Gangloff RP, Scully JR. Hydrogen trap states in ultrahigh-strength AERMET 100 steel. *Met Mater Trans A* 2004;vol. 35(3):849–64.
- [86] Simoni L, Falcade T, Ferreira DC, Kwietniewski CE. An integrated experimental and modeling approach to determine hydrogen diffusion and trapping in a high-strength steel. *Int J Hydrog Energy* 2021;46(50):25738–51.
- [87] Di Stefano D, Nazarov R, Hickel T, Neugebauer J, Mrovec M, Elsässer C. First-principles investigation of hydrogen interaction with TiC precipitates in α -Fe. *Phys Rev B* 93(18). publisher: American Physical Society (APS).
- [88] Drexler A, Depover T, Leitner S, Verbeken K, Ecker W. Microstructural based hydrogen diffusion and trapping models applied to Fe–C X alloys. *J Alloys Compd* 2020;826:154057.
- [89] Wang Y, Connétable D, Tanguy D. Influence of trap connectivity on H diffusion: Vacancy trapping. *Acta Mater* 2016;103:334–40, publisher: Elsevier BV.